Nanocluster-antibody-drug conjugates (NADC) as an intravesical precision theranostic agent for interstitial cystitis

Zhijun Lin[1,#], Wanyan Wang[2,#], Dingxin Liu[1,3], Zhifeng Xu[4], Zhiming Wu[1], Xiangfu Zhou[5], Xiaodong Zhang[6], Yong Huang[5], Qi Zhao[1], Jiang Yang[1,*]

Affiliations:

[1]State Key Laboratory of Oncology in South China, Guangdong Provincial Clinical Research Center for Cancer, Sun Yat-sen University Cancer Center, Guangzhou, 510060 China

[2]Department of Ecosystem Science and Management, Pennsylvania State University, University Park, PA, 16802 USA

[3]Department of Intensive Care Unit, Sun Yat-sen University Cancer Center, Guangzhou 510060, China

[4]Department of Radiology, The First People's Hospital of Foshan, Foshan, 528041 China

[5]Department of Urology, The Third Affiliated Hospital of Sun Yat-sen University, Guangzhou, 510080 China

[6]Tianjin Key Laboratory of Brain Science and Neural Engineering, Academy of Medical Engineering and Translational Medicine, Tianjin University, Tianjin, 300072 China

[#]These authors contributed equally

*Corresponding author: yangjiang@sysucc.org.cn

Abstract

Interstitial cystitis (IC) is a chronic inflammatory disorder characterized by recurring severe pain in the bladder and surrounding pelvic areas, lacking timely diagnostic and therapeutic options. Here, we propose a unitary theranostic nanocluster-antibody-drug conjugate (NADC) by covalently placing dihydroorotate dehydrogenase inhibitors (DHODHi) and ultrasmall gold quantum clusters (AuQCs) on a nerve growth factor (NGF) antagonistic antibody with simultaneous X-ray computed tomographic and near-infrared fluorescence imaging contrasts. Combining anti-inflammatory effects from all individual components, intravesical NADC specifically homed to bladder mucosal lesions and capably alleviated inflammation in chronic, acute, and prophylactic IC models of rats, as revealed by behavioral and pathological evaluations. Transcriptomics unveiled cytokine modulation and concomitant inhibition of perturbed IL-17, NF-κB, TNF, and JAK-STAT signaling pathways. Interestingly, the NADC reconstructed the host bladder microbiota by differentially varying anti-inflammatory and pro-inflammatory bacteria diversities. Distinct from conventional nanoparticles conjugated with antibodies and drugs, NADC relies on the antibody framework and represents a state-of-the-art category of precision theranostic agents with translational potential for diagnosing and treating IC patients.

Keywords: antibody-drug conjugate (ADC); intravesical therapy; interstitial cystitis; gold nanoclusters; theranostics; multimodal imaging; bladder microbiota

Introduction

Interstitial cystitis/bladder pain syndrome (IC/BPS) is a prevalent and chronic disease with overloaded healthcare expenses but without a cure at present[1]. IC patients suffer from debilitating pelvic pain, bladder pressure, and urinary frequency and urgency resulting from bladder lining inflammation. Lacking definitive biomarkers, the diagnosis of IC is rather complex, mandating a combination of tests including but not limited to bladder diary reference, pelvic exams, cystoscopy, potassium sensitivity tests, urine cytology, and even invasive biopsy[2]. However, with unelucidated etiology and symptoms overlapping with other urinary disorders, IC is frequently underdiagnosed or misdiagnosed, left with limited therapeutic options. Represented by clinically approved Rimso-50 dimethyl sulfoxide (50% DMSO), localized intravesical therapy has been proven to be advantageous over oral medications, nerve stimulation, and surgery due to reduced systemic side effects, enriched local concentrations of drugs, high response rates, and minimized invasiveness[3]. Nevertheless, current intravesical therapies, such as guideline-recommended lidocaine, heparin, and DMSO, only provide temporary symptom relief and risk systemic toxicity through leaking into circulation. Moreover, these intravesical agents demand frequent instillations owing to low bladder retention, urinary washout, and poor urothelium entry, which significantly reduce therapeutic efficacy[4]. Therefore, there is a pressing need to develop IC-specific targeted agents to achieve sustained efficacy, preferably with imaging features to reliably diagnose IC, visualize drug distribution patterns, and reduce unnecessary examinations.

Ideal IC management should bilaterally direct anti-inflammation and relieve pain. The nerve growth factor (NGF) is expressed as a pain mediator in bladder tissues through sensitizing afferent nerve pathways associated with IC[5]. NGF inhibitors like tanezumab, fulranumab, and fasinumab have demonstrated clinically meaningful benefits in pain resolution in IC patients[6]. However, as observed in clinical studies, intravenous administration of these monoclonal antibodies inevitably arouses severe systemic toxicity, such as headaches, upper respiratory tract infection, increased joint damage, and peripheral neuropathy, which bring about safety concerns and jeopardize regulatory approvals but could be circumvented via intravesical routes[6]. Meanwhile, non-invasive intravesical therapy can preserve high local concentrations of drugs by direct exposure. Recent studies revealed the anti-inflammatory and immunomodulatory effects of selective dihydroorotate dehydrogenase inhibitors (DHODHi) via suppressing mitochondrial pyrimidine synthesis, exemplified by clinically investigational vidofludimus (IMU-838)[7]. While elevated levels of interleukin (IL)-17A are found in the bladder tissues and urine of IC patients, IL-17A triggers the release of other pro-inflammatory cytokines[8]. Immunosuppressive vidofludimus can downregulate the expression of IL-17A by inhibiting the downstream NF-κB signaling pathway to attenuate chronic inflammation and autoimmune tissue damage[8]. Unfortunately, the indication of vidofludimus has not been expanded to treat IC.

The clinical success of antibody-drug conjugates (ADCs) as a targeted therapy has gone beyond oncology, with investigational examples like ABBV-3373 and DSTA4637S[9, 10, 11, 12].

Even though ADCs and derivatives, including immune-stimulating antibody conjugates (ISAC) and immune-modulating antibody-drug conjugates (IM-ADC), can enhance efficacy and minimize off-target side effects on normal tissues by precision targeting, they lack the visualizability of treatment surveillance. In this study, we covalently engineered an intravesical theranostic nanocluster-antibody-drug conjugate (NADC), comprised of an NGF-targeting monoclonal antibody, immunosuppressing DHODHi, and gold quantum clusters (AuQCs) (Fig. 1). Unlike conventional nanoparticles (NPs), ultrasmall AuQCs are comparatively insignificant in size with reference to antibodies and exhibit anti-inflammatory effects and imaging contrasts of non-invasive near-infrared fluorescence (NIRF) and spectral computed tomography (CT). The NADC unifies the otherwise differential pharmacological behaviors of individual drugs to achieve image-guided therapeutic synergy against IC. The combined locoregional bladder instillation and specific NGF targeting of NADCs can maximize drug precision, minimize systemic toxicity, and spare normal tissues, improving somatic pain symptoms and functional voiding in rat models of chronic, acute, and prophylactic IC. Analyses of the transcriptome and microbiome identify multifaceted inhibition of inflammatory signaling pathways of interleukin-17 (IL-17), nuclear factor-κB (NF-κB), tumor necrosis factor (TNF), and Janus kinase-signal transduction and activator of transcription (JAK-STAT) and differential modulation of dysregulated microbiota populations in IC. The versatile NADC framework represents theranostic convergence of synergistic precision medicine that can safely and effectively treat IC with high NGF expressions in bladder mucosae under image guidance.

Results

Preparation and characterization of NADCs

To synthesize NADCs, we utilize a two-step conjugation strategy (Fig. 1a). First, a proportion of amines on tanezumab were sulfhydryl-activated by Traut's reagent. In parallel, AuQCs were covalently coupled to the amine-reactive *N*-hydroxysuccinimide (NHS) ester of a hetero-bifunctional sulfo-SMCC to form stable amides. Next, the thiolated anti-NGF antibody reacted with maleimide-tethered AuQCs to derive thioether bonds. Last, the remaining primary amines of the complex were covalently crosslinked to the benzoic acid of vidofludimus with NHS-EDC to attain NADC. Accompanied by sequential modifications of tanezumab by AuQCs and DHODHi, we observed increases in the hydrodynamic size from 7.5±0.5 to 28.2±4.5 nm and the zeta potential from -7.6 ± 0.7 mV to -16.7 ± 0.7 mV (Fig. 2a,b). While AuQCs were ultrasmall under 3 nm as visualized by transmission electron microscopy (TEM), NADC reached 25 nm in diameter due to the relatively large size of immunoglobulins (Fig. 2c,d and Supplementary Fig. 1). NADC well-preserved characteristic absorption peaks of DHODHi at 260 and 290 nm, as well as the anti-NGF peak at 280 nm that was broadened by AuQCs conjugation (Fig. 2e).

Furthermore, a minor hypsochromic shift in the NIRF emission of AuQCs was perceived following covalent modifications into AuQCs-anti-NGF or NADC (Fig. 2f). We then calculated the molar nanocluster-to-drug-to-antibody ratio (NDAR) to be 4.7:3.4:1, which warrants dual DHODHi and theranostic AuQCs payloads to concurrently alleviate overactive immune reactions and navigate diagnostic imaging (Fig. 2g). Notably, given the relative dimensions of individual constituents in the complex, the NDAC is fundamentally dissimilar with conventional antibody-and-drug-conjugated NPs (Fig. 2h).

Structures and binding affinities of anti-NGF antibodies are retained in NADC

Far-ultraviolet circular dichroism (CD) spectroscopy revealed the dominant contribution and rigid preservation of antibody secondary structures in NADC, with largely unaltered β-sheets at 216 nm, β-turn broad bands at 220-230 nm, and flexible random coils at 200 nm (Fig. 2i). Notwithstanding the dominance of tanezumab in CD signatures of NADC, α-LA in AuQCs still contributed to an elevated α-helix proportion, with ambiguous but distinguishable negative bands at 222 and 208 nm in NADC (Fig. 2i,j). To assess whether antigen recognition and binding are still viable in the NADC scaffold after conjugation with AuQCs and DHODHi, we performed label-free biolayer interferometry (BLI) to analyze interference patterns upon interactions with NGF (Fig. 2k). Real-time BLI sensorgrams of the anti-NGF antibody and NADC rendered coinciding steps in the loading, association, and dissociation phases, suggesting resembling probe immobilization and antigen-antibody binding kinetics (Fig. 2l). In the meantime, minimal interactions were observed in all phases for bovine serum albumin (BSA). After probe immobilization on the sensor surface, affinity binding dynamics were measured for anti-NGF and NADC at gradient NGF concentrations ranging from 31 to 500 nM (Fig. 2m-p). Fitting of maximum wavelength shifts by Michaelis-Menten substrate-binding kinetics yielded equilibrium dissociation constants (K_D) of 4.019×10^{-9} M for anti-NGF and 8.505×10^{-9} M for NADC at equivalent orders of magnitude (Fig 1n,p). Collectively, these results elaborated on the successful preparation of NADC with the rigid antibody conformations and NGF-targeting affinities sufficiently retained as the prerequisite for subsequent IC theranostics.

NADC as a dual-modality imaging contrast agent for IC

To scrutinize the diagnostic features of NADC, we administered the NADC agent by intravesical instillation to rats with cyclophosphamide (CYP)-induced urinary bladder inflammation, a well-established preclinical IC model. AuQCs and NADC could readily delineate bladder contours with fast contrast enhancement in a trice (Fig. 3a,b). Time-course NIRF imaging revealed a classic one-compartment open model, where administered contrast agents were instantaneously distributed in the inflamed bladder as a uniform body compartment. In rats with IC, AuQCs were rapidly cleared with only minor NIRF signals seen after 3 h, whereas NADC was dynamically sustained with prolonged retention and identifiable signals even after 12 h (Fig. 3a). The bladder retention half-life of

NADC was experimentally determined to be 4.6±0.3 h, much higher than 1.2±0.1 h of AuQCs (Fig. 3b). In contrast, the NIRF intensities of both NADC and AuQCs instantly and similarly decayed in healthy rats within 3 h post-instillation, with comparable half-lives of 1.5± 0.2 h and 1.6 ± 0.2 h, respectively (Fig. 3c,d). The results authenticated that the antibody-directed NGF-targeting NADC could extend retention in the IC-irritated bladder with an improved diagnostic window and drug action.

As in human IC, local NGF at the inflammation sites in the preclinical IC rat model was overly expressed with higher signals from immunofluorescence than in normal bladders[13] (Fig. 3e,f). 12 h after intravesical injection, the retained NIRF signal of NADC in bladder tissues was much higher than that of AuQCs, in extensive and precise colocalization with NADC-targeted NGF. Three-dimensional (3D) volumetric imaging by Z stacks visually showed stronger, broader, and more penetrative NIRF signals of NADC, dictating long bladder residence time and partial penetration into deep bladder urothelia by actively targeting NGF (Supplementary Fig. 2).

On top of NIRF, the intrinsic CT contrast of NADC overcomes the limited tissue penetration depth as a complementary imaging modality, providing cross-sectional information and reinforced anatomical microstructures (Fig. 3g). Taking advantage of multi-energy spectral CT, phantom images of AuQCs and NADC in equivalent contrast can be clearly distinguished from the clinical iodine agent, Ioversol, with only minor crosstalk bleeding through iodine and non-iodine mapping (Supplementary Fig. 3a,b). The monochromatic energy attenuation curves of AuQCs and NADC are almost identical within 40-140 keV, with considerable differences in keV energy separation to discriminate Au from PBS and iodine (Supplementary Fig. 3c). The comparable CT signal intensities of AuQCs (R^2=0.99) and NADC (R^2=0.98) could be decomposed, linearly depending on concentrations of Au material densities with low interference from Ioversol in non-iodine projections (Fig. 3h,i). After intravesical instillation in healthy and IC rats, bladders were immediately delineated by contrast-enhanced spectral CT using AuQCs and NADC (Fig. 3j). Time-lapse CT imaging affirmed a more deferred bladder voiding in IC rats administered with NADC than AuQCs, while expeditious emptying of both agents was found in healthy rats (Fig. 3k,l). Combining the bimodalities of NIRF and spectral CT with contrast enhancement from NADC allows us to register temporal and spatial resolutions simultaneously to diagnose bladder disorders such as IC.

Limited bladder lining permeability of NADC into systemic circulation towards SV-HUC-1 mimicry, rat, and human urothelia

As probed earlier by 3D volumetric imaging, NADC capably pervaded the inner bladder lining and reached the suburothelium at a concrete penetration depth (Supplementary Fig. 2). We adapted the Ussing Chamber model to ascertain whether NADC possesses impermeability traits without traversing bladder tissues and triggering unintended side effects from systemic entry and absorption. First, we constructed an in vitro bladder mucosa mimicry using the immortalized human normal urothelial cell line SV-HUC-1 (Supplementary Fig. 4a). SV-HUC-1 was continuously cultured until a monolayer of high

confluence and tight junctions formed and reached saturated transepithelial/transendothelial electrical resistance (TEER) to mimic urothelium (Supplementary Fig. 4b). Next, we added AuQCs and NADC from the apical or basolateral side and then periodically monitored NIRF of the opposite sides to scrutinize whether the agents were transported across urothelium from transcytosis or paracellular space (Supplementary Fig. 5). Noticeably, NIRF signals were only observed at the ipsilateral application side but not at the contralateral side, confirming the physiological impermeability of SV-HUC-1 urothelial mimicry for both AuQCs and NADC. Likewise, we collected bladder tissues from healthy and IC rats and established ex vivo urothelia in the Ussing Chamber to evaluate the permeability (Supplementary Fig. 6,7). Surprisingly, besides the intact bladder mucosa from healthy rats, the irritated bladder urothelium from IC rats undergoing barrier disruption was neither penetrable to AuQCs nor NADC. Last, we set up a similar transepithelial ex vivo model using surgically dissected human bladder tissues with histological and microenvironmental organ characteristics of clinical relevance (Fig. 4). Consistently, AuQCs and NADC were retained at the ipsilateral side and unable to cross the bladder barrier.

NADC alleviates in vitro inflammatory responses

Before initiating in vivo studies, we verified if NADC could alleviate in vitro inflammatory responses in cells. We activated NOD-like receptor protein 3 (NLRP3) inflammasomes in SV-HUC-1 bladder epithelial cells to mimic inflammatory responses synergized by lipopolysaccharide (LPS) and adenosine triphosphate (ATP). Measured by quantitative reverse transcription polymerase chain reaction (RT-qPCR), LPS/ATP co-induction upregulated mRNA expression of pro-inflammatory cytokines of IL-1β, TNF-α, and IL-6 and downregulated anti-inflammatory cytokines of IL-4, IL-10, and IL-13 in the stimulated SV-HUC-1 model (Supplementary Fig. 8). Fortunately, the inflammation-induced differential cytokine expressions were effectively ameliorated by NADC, with each NADC constituent of tanezumab, DHODHi, and AuQCs also actively imposing therapeutic mitigation to some extent.

NADC as a therapeutic agent to treat chronic interstitial cystitis in rats

Next, we estimated the in vivo therapeutic efficacy of NADC in a standard chronic IC rat model established by repeated intraperitoneal (i.p.) CYP induction (Fig. 5a). During the entire therapeutic process, we applied the Von Frey rodent test with a calibrated filament to determine the mechanical sensitivity threshold from lower abdomen withdrawals in response to a punctate stimulus (Fig. 5b). Meanwhile, we carried out time-course bladder urodynamics to meticulously track urinary voiding functions (Fig. 5c). After IC onset by repetitive low-dose CYP stimulations, the mechanical withdrawal threshold in the IC rat models was reduced and consistently maintained at a low level with a prominent reflex over the entire period, indicative of persistent, severe lower abdominal pain (Fig. 5d). Nonetheless, intravesical therapy with NADC effectively attenuated pain symptoms and almost reversed the mechanical allodynia threshold of IC to normal levels, with individual NADC components exerting partial yet significant efficacy (Fig. 5d). Furthermore, urodynamic assessment informed markedly heightened basal and maximum intravesical

pressures alongside increased micturition frequency (Fig. 5e-h), mirroring the clinical presentation of IC patients who experience recurrent urination and urgency. After intravesical therapy, the abnormal urinary symptoms were all rehabilitated partly by tanezumab, DHODHi, and AuQCs but restored to healthy levels with uninfluenced voiding by NADC.

In addition to soothing IC symptoms, NADC also improved bladder macroscopic manifestations through anatomical examination of gross pathology, significantly diminishing IC-triggered congestion, bleeding, and edema (Fig. 5i). Accordingly, the bladder organ index elevated by IC was mitigated by NADC and each constituent (Fig. 5j). Compared to the intact bladder anatomy with high integrity in the normal bladder, inflamed bladder lesions in IC rats featured a disrupted structure with urothelium denudation, submucosal edema, inflammatory infiltration, lamina propria hemorrhage, and granulation, which were adequately attenuated by NADC (Fig. 5k). Further histopathological analyses unveiled palliated outcomes on the index of severity, histological scores, and submucosal thickness by NADC, which were all raised in IC (Fig. 5l-n). The results confirmed intravesical NADC's effectiveness in restoring cystitis-associated pathological damage to bladder tissues.

NADC as a therapeutic agent to treat acute interstitial cystitis (AIC) in rats

Although IC is typically characterized as a persistent and chronic condition, part of patients may experience acute exacerbations of flare-ups with intensified symptoms. To evaluate the NADC efficacy against the exacerbated condition[14], we constructed an AIC rat model induced with a high dose of CYP (Fig. 6a). As measured by the Von Frey test, the 50% mechanical withdrawal threshold of AIC rats was rapidly curtailed within 4 days, reflecting severe hyperalgesia (Fig. 6b,c). Meanwhile, the body weight of AIC rats sharply dropped in short periods (Fig. 6d). To explore the influence of AIC on locomotor activities and anxiety-like behaviors of rats, we performed the open field test (OFT) and tracked the exploration footage using an overhead camera (Fig. 6e). Healthy rats moved freely in all zones of the arena with abundant footage, but rats suffering from AIC-induced pain were crouched with deficient total traveled distance, low max velocity, and restricted locomotor areas (Fig. 6e-i). The willingness, capability, and rate of motor activities were affected by the visceral pain from AIC. By comparison, intravesical therapy of NADC substantially recovered the mechanical allodynia, body weight loss, and diminished locomotor parameters, with individual NADC constituents also being moderately effective in cystitis remission (Fig. 6). Additionally, the urinary function of AIC rats was verified by urodynamic testing (Fig. 6j). Notably, the aggravated basal and maximum bladder pressures and urination frequency in AIC rats were significantly alleviated with intravesical instillation, with the most pronounced therapeutic effect observed for NADC (Fig. 6k-m). Gross pathology unveiled more hemorrhagic lesions and more prominent edema in the bladder mucosa of AIC rats (Supplementary Fig. 9a) than in chronic IC (Fig. 5i), which were effectively mitigated by intravesical therapy. Correspondingly, the bladder submucosal edematous zone markedly thickened and hemorrhaged by AIC was microscopically visualized to be improved by the NADC intravesical intervention (Supplementary Fig. 9b).

Aligned with earlier results on chronic IC, the elevated organ index, severity, and histological score in AIC were suppressed (Supplementary Fig. 9c-e).

NADC as prophylactic therapy for IC in rats

Gleaned from anti-microbial agents for prophylactic therapy of bacteria-associated cystitis, we aim to study the revelation of intravesical NADC as non-surgical and minimally invasive prophylaxis for IC. Before the high-dose CYP induction to recapitulate exacerbated cystitis in rats on the 6th day, we perfused the bladder with intermittent prophylactic NADC at pre-defined dosing (Fig. 7a). Coinciding with its therapeutic effects in chronic IC and acute cystitis, pre-dosed NADC exhibited appreciable preventative efficacy on the mechanical pain threshold, body weight changes, urodynamics, bladder pressures, and micturition frequency deteriorated from cystitis onset (Fig. 7b-g). Specifically, urination occurred 4 times in 30 min in normal rats, 13 times in rats with acute cystitis, and 5 times with NADC prophylaxis (Fig. 7d). Macro- and microscopic histopathological analysis of the bladder further verified the prevention of cystitis-related bladder injuries by NADC prophylaxis, with insignificantly altered organ index, severity, and histological score concerning healthy rats (Fig. 7h-l). Notably, each NADC unit, i.e., vidofludimus, tanezumab, and AuQCs, was competent in counteracting acute cystitis induction.

Coordinative molecular mechanisms of NADC

Although the mechanism of action for NADC is straightforward via dual selective inhibition of DHODH and NGF, the downstream and synergistic pathways remain underexplored. In addition, AuQCs manifested theranostic features with comparable therapeutic and prophylactic efficacies (Fig. 5-7). To inspect the underlying molecular mechanisms of the NADC complex against IC, we profiled transcriptomes of bladders dissected from IC rats treated with PBS or NADC by RNA sequencing (RNA-seq) with reference to healthy controls. The high-dimensionality RNA-seq data were dimensionally reduced by principal component analysis (PCA), distinctly separating the IC group by differentially expressed genes (DEGs) from the converged healthy control and IC rats receiving intravesical NADC treatment (Fig. 8a). The number of DEGs altered by IC among all genes increased in both up- and down-regulated directions, which were extensively restored by intravesical NADC instillation (Fig. 8b). In particular, the plentiful DEGs downregulated by IC were overturned into augmented expressions by NADC. We then mapped the DEGs for enrichment analyses of gene ontology (GO) and Kyoto Encyclopedia of Genes and Genomes (KEGG) (Fig. 8c, d). GO informatics highlighted enriched slim annotations of IC for response to external stimulus, generation of reactive oxygen species (ROS), response to chemical, and ROS-modulated enzyme activities, while NADC assimilated GO terms of cytokine and cytokine receptor activities, cytokine production, growth factor receptor binding and activity, inflammatory response, immune response, cellular response to tumor necrosis factor (TNF), interleukin-6 (IL-6) production, and ROS metabolism (Fig. 8d). Next, miscellaneous KEGG cascades noted for cytokine regulation, immune modulation, neuroactive ligand-receptor interaction, glycolysis/gluconeogenesis, and inflammation were enriched (Fig. 8c), comprehensively covering the combinational effects of NGF and

DHODH dual inhibitions and immune-modulating AuQCs. Compared to their larger-sized counterparts, ultrasmall nanoclusters AuQCs have been widely reported to scavenge ROS and attenuate inflammation with enhanced catalytic activities[15]. Importantly, we highlighted coordinative admitted inflammation signaling pathways of IL-17, NF-κB, and JAK-STAT that were dysregulated by IC but effectively mitigated by NADC with opposite regulations (Fig. 8e). Key quality-control passed gene panels of these inflammation pathogenic pathways in the bladder transcriptome significantly altered by IC were rescued by NADC and almost restored to control levels (Fig. 8f and Supplementary Fig. 10), suggestive of IC relief. Protein-protein interaction network analysis modeled the complex pathways and biological functions, which distinctly disclosed the interconnected signaling pathways shared with interacting nodes (Supplementary Fig. 11, 12).

To complement transcriptional analysis, we further interrogated protein expressions of key effectors in the pinpointed pathways by immunoblotting. In consistency with IF results (Fig. 3e,f), NGF was overly expressed with CYP induction in IC bladder tissues of rats to provide a viable precision target for NADC (Supplementary Fig. 13). Interestingly, none of the agents suppressed the aberrant NGF expression, including NGF-targeting tanezumab and NADC, corroborating a sustained targeting efficiency. In contrast, the phosphorylation of the transmembrane NGF catalytic receptor and pain sensory mediator, tropomyosin receptor kinase A (TrkA), was incremented in IC but inhibited by tanezumab and NADC, with total TrkA remaining identical in healthy and IC rats and independent of therapeutic interventions. Next, we probed major pro-inflammatory cytokines and observed potent inhibition of IL-17A, IL-6, and IL-1β by DHODHi and TNF-α by AuQCs in NADC, with negligible effects from anti-NGF (Supplementary Fig. 13). As the upstream regulator, IL-17A is a known target of vidofludimus that impairs NF-κB and JAK-STAT pathways[16]. After that, we comprehensively screened pivotal mediators in NF-κB and JAK-STAT pathways at protein levels (Supplementary Fig. 14). Defectively elevated phosphorylation of the two IκB kinase (IKK) catalytic subunits, IKKα and IKKβ, and RelA/p65 resulted in activated canonical NF-κB in IC models, which was adequately inhibited by NADC to limit degradation of the NF-κB inhibitor IκBα[17], yet with minimal influence on the total protein expressions. Likewise, IC-deregulated JAK-STAT members broadly involved in cytokine signaling, including JAK1, STAT1, and STAT2, were appreciably attenuated by NADC with potent synergy, which concurrently prohibited phosphorylation and expression.

Alleviation of IC through bladder microbiota modulation by NADC

Although the bladder microbiome is less diverse and traditionally overlooked, emerging clinical evidence has established a plausible correlation between urinary microbiomes and IC/BPS[18]. To investigate whether NADC mitigated IC through leveraging bladder microbiota, we isolated bacterial DNA from rat bladder tissues and ran 16S ribosomal RNA (rRNA) gene amplicon sequencing. Using non-metric multidimensional scaling (NMDS) analysis of Bray-Curtis dissimilarity distances, we identified a distinct bladder microbiota in IC rats significantly differing from all the other treatment groups ($P<0.05$) that shared high similarities with the healthy control (Fig. 9a). Comparatively, DHODHi monotherapy induced a more extensive segregation of microbiome alteration. At genus

levels, we found significant divergence of the IC microbiome from that of healthy rats in the composition and abundance (permutational multivariate ANOVA testing, Pr(>F)=0.02), with overrepresented genera like *Escherichia*, *Shigella*, *Enterococcus*, *Staphylococcus*, and *Enterobacter* and underrepresented genera like *Acinetobacter*, *Burkholderia*, *Caballeronia*, and *Paraburkholderia* (Fig. 9b). The number of observed operational taxonomic units (OTUs), Chao1, and ACE indices in the alpha-diversity metrics were significantly reduced in IC and anti-NGF treatment groups but were rescued to normal levels with treatment of AuQCs, DHODHi, or NADC (Fig. 9c). Further taxonomic analysis of microbial community compositions of OTUs in bladder tissues validated the conservation of core genera of *Rhodococcus* among all groups, along with decreased abundance in high-prevalence *Acinetobacter* and increased abundance in less-prevalence *Escherichia-Shigella* in IC (Fig. 9d). With linear discriminant analysis (LDA) effect size (LEfSe), cladograms highlighting key bacterial clades portrayed spatial phylogenetic correlations of bacterial lineages in taxonomic hierarchies (Fig. 9e). Noticeably, the bacterial taxa at phylum, class, order, family, and genus levels were all significantly varied by IC to some extents (LDA scores ≥2.0) yet were inversely regulated in a similar clade landscape by intravesical NADC therapy. The relative abundance of *Gammaproteobacteria* (class) and *JG30-KF-CM45* (family to species) with LDA scores ≥3.0 by LEfSe were significantly higher in IC, contributing to pathogenesis (Fig. 9f). In contrast, *Actinobacteriota* (phylum and class), *Nocardiceae* (family), *Rhodococcus* (genus and species), and *Corynebacteriales* (order) were enriched following NADC therapy, which depreciated *Gammaproteobacteria* (class) along with other virulent populations of *Enterobacteriaceae* (family), *Escherichia-Shigella* (genus to species), *Bacilli* (class), and *faecalis* (*Enterococcus* species) (Fig. 9f). Therefore, the bladder microbiome remodeling by NADC plays an indispensable role in IC mitigation.

Safety profiles of NADC

As evidenced by earlier transmembrane and imaging studies (Fig. 3 and Supplementary Fig. 4-7), catheter-directed intravesical NADC was refrained from penetrating bladder tissues and entering the systemic circulation, theoretically with minimized systemic toxicity. To verify such claims, we scrutinized toxicity profiles of intravesical NADC and individual drug payloads by comprehensively screening panels of clinical chemistry and hematology. Electrolyte balances of bicarbonate (CO_2), K^+, Na^+, Cl^-, and Ca^{2+} were well maintained (Supplementary Fig. 15). Additionally, indicators of liver and kidney functions, such as alanine transaminase (ALT), aspartate transaminase (AST), alkaline phosphatase (ALP), lactate dehydrogenase (LDH), blood urea (UREA), and creatinine (CREA), all fell within reference ranges without significant changes from the control. Blood proteins of albumin (ALB), globulin (GLB), and total protein (TP) stayed normal. The complete blood count (CBC) covering red blood cells (RBC), white blood cells (WBC), and platelets (PLT) in all groups lay in biologically non-significant reference ranges, despite a minor elevation of basophils (BAS) observed with NADC treatment (Supplementary Fig. 16).

Discussion

The psychological impact of IC is pervasive, long-lasting, and debilitating, with frequent

urination and pain negatively interfering with social intimacy, work, and daily activities. Nonetheless, practical, accessible, and affordable therapy for IC is somewhat limited in clinical practice. As a relatively emerging therapeutic modality, ADC combines the specificity of monoclonal antibodies and the cytotoxic potency of drug payloads, necessitating precise delivery and selective killing to tackle otherwise unsolvable clinical challenges. While there are fifteen ADCs approved by the US Food and Drug Administration and more in clinical phases poised to enter the market, indications are predominantly limited to hematologic malignancies and solid tumors, with autoimmune conditions primarily overlooked. Cytotoxic payloads of ADCs are unsuitable for treating IC, where the therapeutic objective is to direct immune modulation or suppression rather than causing cell death. Besides, all current ADC drugs lack a companion imaging modality to inform their pharmacokinetics and drug distribution patterns. As an imaging facilitator, AuQCs afford intrinsic NIRF with a significant Stokes shift arising from band gap discretization and optical quantum confinement, aside from the high atomic number (Z=79) and K-edge (80.7 keV) of Au as superior CT contrast[19]. Besides whole-body in vivo imaging (Fig. 3), the NADC is also liable for microscopical visualization of drug distribution patterns in high resolution. Interestingly, despite the weaker signal, the distribution of AuQCs without antibody-mediated targeting was also confined in regions with NGF expression, probably by passive targeting (Fig. 3).

Therefore, intravesical NADC polytherapy enables visualizable precision medicine for IC, combining catheter-guided direct dosing of high drug concentrations, NGF-specific targeting, selective DHODH modulation, and theranostic AuQCs. Compared to systemic administration, intravesical instillation delivers a fixed dose relatively independent of body weight, raising local drug concentrations in the dysfunctional bladder more rapidly. The stringently controlled infusion rate can reduce infusion-related reactions and hypersensitivity. A non-cleavable covalent linkage of stable amide and thioether bonds in NADC prevents the premature release of active DHODHi and AuQCs and warrants cytosolic efficacy after antibody degradation. It has been reported that ADC with a thioether covalent linker is more effective in proliferating cancer cells with higher activities than a disulfide cleavable counterpart[20]. Therefore, such a structural design can improve in vivo stability, therapeutic window, and pharmacokinetics of payloads. In the study, the multifold precision of NADC by intravesical drug dosing spared normal bladder tissues with low urothelial NGF expression and immunologically modulated inflammatory cells with non-cytotoxic payloads of vidofludimus and AuQCs. Although the bladder mucosal urothelium is a multifaceted tight-junction barrier known as one of the most impermeable membranes of the body, patients with IC conditions may experience increased bladder permeabilities[21]. As verified by whole-body imaging and Ussing chamber assays (Fig. 3-4 and Supplementary Fig. 4-7), the limited bladder permeability of NADC serves as a prerequisite of locoregional intravesical therapy without entering systemic circulation or compromising urothelial integrity and detrusor muscles. Consequently, the direct relief of inflamed bladder linings by intravesical NADC can bypass drug overdose and improve patient tolerance, resulting in minimized off-target toxicity (Supplementary Fig. 15-16).

Meanwhile, the drug antibody ratios (DAR) of AuQCs and DHODHi fall around optimal DAR values between two and four for most ADCs with balanced safety and efficacy[22], ensuring appreciable therapeutic efficacy on the mechanical threshold and micturition function against chronic IC and AIC (Fig. 5-6). Gleaned from anti-microbial agents for the prophylactic therapy of bacteria-associated cystitis, we also studied the revelation of intravesical NADC as non-surgical and minimally invasive prophylaxis for IC. The intravesical prophylactic therapy with NADC prevented pain symptoms and bladder dysfunction from acute cystitis to limit its occurrence and recurrence (Fig. 7). Following receptor-mediated internalization to release AuQCs and vidofludimus payloads, NADC concurrently inhibits multiple inflammatory pathways such as NF-κB, JAK-STAT, IL-17, and TNF as combinatorial precision therapy (Fig. 8c-f), which was well-documented with clinical success[23, 24]. As a promising transformative therapeutic, NADC also provides alternative mechanisms toward IC alleviation by reshaping the bladder microbiome in composition and abundance (Fig. 9). The altered bacteria with endosymbiosis are widely involved in bioremediation, biosynthesis, and regulation of inflammation[25, 26].

In summary, we report for the first time a theranostic intravesical NADC with immunomodulating drug payloads in non-cleavable covalent linkage, serving as a unified multifaceted precision agent against chronic, acute, and prophylactic IC symptoms through catheter guidance. Besides the ability to be tracked by imaging, the NADC simultaneously regulates multiple perturbed inflammation-related signaling pathways and remodels the host bladder microbiota. Our findings here provide new insights into the development and in vivo visualization of theranostic ADCs, which may be further extended to a broader category of ADCs, peptide-drug conjugates, aptamer-drug conjugates, and other relevant conjugates to treat autoimmune diseases in general.

Methods

Chemicals

High-purity α-LA with a low calcium content (<0.055%) was acquired from Agropur. Gold chloride trihydrate ($HAuCl_4 \cdot 3H_2O$), cyclophosphamide (CYP), and lipopolysaccharides (LPS) were purchased from Sigma-Aldrich. Vidofludimus, sulfosuccinimidyl-4-(*N*-maleimidomethyl)cyclohexane-1-carboxylate (sulfo-SMCC), adenosine 5′-triphosphate (ATP), *N*-(3-dimethylaminopropyl)-*N*′-ethylcarbodiimide hydrochloride (EDC), and *N*-hydroxysuccinimide (NHS) were purchased from MedChemExpress. The anti-NGF therapeutic monoclonal tanezumab was purchased from Absin Bioscience. 2-Thiolanimine hydrochloride (Traut's reagent) was obtained from Shanghai Aladdin.

Synthesis and characterization of NADC

AuQCs with optimal NIR fluorescence were synthesized as previously reported[27]. Briefly, 40 mg mL^{-1} α-LA and 10 mM $HAuCl_4$ were mixed at equivalent volumes. After that, 1 M NaOH at 15% (v/v) was added to the mixture and sufficiently vortexed until the precipitates formed from the prior step were completely dissolved. The reaction then

proceeded with stirring at 40 °C for 20 h and was dialyzed against pH 7.4 PBS at 10 kDa molecular weight cutoff for 2 days. The dialysis was sealed from light with fresh buffers substituted every 8 h. The concentration of AuQCs was quantitatively measured by nanoparticle tracking with a NanoSight NS500 system (Malvern Panalytical).

To prepare the NADC, we first modified tanezumab with ultrasmall AuQCs[28]. Typically, 20 μg tanezumab in 100 μL PBS reacted with 26.6 μM Traut's reagent at room temperature for 1 h to modify primary amines into reactive sulfhydryl groups. In parallel, 30 μM water-soluble sulfo-SMCC was added to 6 μM AuQCs in PBS and maintained for 30 min at room temperature to drive amide bond formation between NHS esters and primary amines of AuQCs. After washing with PBS by 3 kDa ultrafiltration (Millipore), the sulfhydryl-activated tanezumab reacted with maleimide-modified AuQCs by the hetero-bifunctional sulfo-SMCC for 2 h in the dark at 4 °C, resulting in the stable formation of thioether bonds (Fig S1). To remove unreacted AuQCs, we extensively washed the modified complex with PBS via 100 kDa ultrafiltration (Millipore). Last, the remaining unreacted amines in the complex were covalently conjugated to the benzoic acid of vidofludimus to acquire NADC. 20 μM equimolar NHS and EDC were appended into 25 μM vidofludimus and kept for 15 min at room temperature[29]. Afterward, activated vidofludimus was added to AuQCs-modified tanezumab and incubated for 2 hours at room temperature from light. Excessive vidofludimus small molecules in the reaction were eliminated by 3 kDa ultracentrifugation.

The morphology and size were characterized using a Philips CM-200 TEM at 200 kV. UV-vis absorption spectra were recorded with a UV-2600 spectrophotometer (Shimadzu). Fluorescence measurements were recorded with a Tecan Infinite M200 plate reader. Dynamic light scattering (DLS), zeta potentials, and PDI were measured by Zetasizer Nano ZSE (Malvern Panalytical). CD spectra were monitored with an Aviv 62DS circular dichroism spectrometer (Aviv Biomedical), and secondary structure compositions were determined using the beta structure selection (BeStSel) approach.

Biolayer interferometry assays

To confirm the binding affinity between NADC and NGF after conjugation, we performed label-free BLI analysis using the Octet R8 system (Sartorius)[30]. First, the anti-human IgG Fc capture (AHC) biosensor (Sartorius) was conditioned in the detergent-containing Kinetic Buffer (KB, PBS with 0.02% v/v Tween-20) for 60 s. Next, 75 μg mL^{-1} NADC or tanezumab on an equivalent antibody basis was immobilized onto the AHC biosensor surface for 60 s. Gradient NGF concentrations from 31 to 500 nM were bound to the modified biosensor during the association process, followed by dissociation in KB. The equilibrium dissociation constant (K_D) was calculated from the binding curves in the Octet Analysis Studio software (Sartorius).

TEER measurement of uroepithelium

The human normal urothelial cell line SV-HUC-1 used in this study was from the Cell Resource Center of the Chinese Academy of Sciences (Shanghai, China). The integrity

and permeability of cellular monolayers were tested with immortalized human uroepithelial SV-HUC-1 cells by seeding into the upper chambers of 12-well plates at a density of 5 × 10^4 cells per well. Over time, TEER was periodically measured with the RE1600 Epithelial Volt/Ohm Meter (Beijing Jingshi Technology). After continuous growth of cells to reach stabilized TEER, the upper chamber membranes with epithelial cells were used for Ussing chamber assays[31]. TEER is calculated as follows:

$$TEER = (R1 - R0)/0.33$$

Where 0.33 is the surface area of the upper membrane, R0 is the TEER value of a cell-free insert, and R1 is the TEER value of an insert with cells forming stabilized tight junctions.

Ussing chamber assays

To evaluate the mucosal drug transport of NADC across SV-HUC-1 mimicry, rat, and human urothelia, we carried out the Ussing chamber assays in a setup consisting of two fluid-filled, heated and aired chambers divided into the apical and basolateral sides. Human bladder tissues were surgically resected from para-cancerous tissues of a bladder cancer patient receiving radical cystectomy at the Sun Yat-sen University Cancer Center under a protocol approved by the ethical committee (#SL-B2023-305-01). Rat bladders were excised from sacrificed rats and extensively washed with cold PBS. Stripped human and rat tissues and the membrane of tight-junction SV-HUC-1 cells from above with an effective exposed area of 0.1 cm^2 were settled in modified Ussing chambers[32]. Krebs-Henseleit Buffer Modified (KHB) was filled in the feeding and reception tanks. The system was continuously oxygenated with O_2/CO_2 (95/5%) and maintained at 37 °C. Next, 500 mM (Au content equivalence) AuQCs or NADC was added to the reception tank. For fluorescence measurement at each time point using a Tecan M200 plate reader, 100 μL solution was taken every 30 min from the feeding and reception tanks and supplemented with identical volumes of fresh solution on both sides.

Cellular mRNA expressions by RT-qPCR

SV-HUC-1 cells were cultured at 37 °C in Ham's F-12K medium (Gibco) containing 10% fetal bovine serum (FBS) in a humidified atmosphere with 5% CO_2. Typically, 2×10^6 SV-HUC-1 cells were seeded in 6-well plates into six groups: control, LPS/ATP, LPS/ATP + anti-NGF antibody (10 μg mL^{-1} tanezumab), LPS/ATP + AuQCs (180 nM), LPS/ATP + DHODHi (300 nM), and LPS/ATP + NADC (10 μg mL^{-1} antibody basis). After 2 h treatment, cells were further stimulated with 10 μg L^{-1} LPS and 2.5 mmol L^{-1} ATP for another 12 h, with total RNA extracted using an RNAprep Pure Cell kit (TianGen Biotechnology). RNA concentrations were calibrated by a NanoDrop 2000 spectrophotometer (Thermo Fisher Scientific). Further, cDNA was synthesized from 1 μg total RNA with a FastKing RT Kit (TianGen Biotechnology) and subject to RT-qPCR. PCR amplification was performed with a RealStar Green Fast Mixture (GenStar) containing hot-start Taq DNA polymerase and SYBR Green I to monitor DNA amplification. Sense and antisense strands of primers were synthesized at Shanghai Sangon Biotechnology using sequences as in Supplementary Table 1. Melting curves were constantly monitored to exclude nonspecific products, and

expression was calculated from the average of triplicates using $2^{-\Delta\Delta Ct}$ with reference to the glyceraldehyde-3-phosphate dehydrogenase (GAPDH) or β-actin controls.

In vivo near-infrared fluorescence imaging

All animal procedures were reviewed and authorized by the Institutional Animal Care and Use Committee (IACUC) at the Sun Yat-sen University Cancer Center (#SYSU-IACUC-2021-000986). Female Sprague-Dawley (SD) rats weighed 220 ± 20 g were regularly kept in a constant environment at 24 °C with a 12-h diurnal cycle. Non-invasive in vivo NIRF imaging was conducted using an IVIS Spectrum system (PerkinElmer). Rats were fasted for 4 h and shaved at the abdominal region before imaging. After intravesical administration of AuQCs or NADC, NIRF images were taken at various time points post-injection under anesthesia and processed by multispectral unmixing to distinguish AuQCs-specific signals from autofluorescence using the Living Image software (PerkinElmer)[33, 34]. The average fluorescence signal intensity of the region of interest (ROI) in the bladder area was calculated following the identification from bright-field images.

In vivo spectral CT imaging

Dual-energy CT imaging was performed using a GE Revolution CT scanner with GSI Xtream (GE Healthcare). Monochromatic images were captured in a 40–140 keV fast-switching energy range and processed in the GSI Viewer software (GE Healthcare) to reconstruct composite images following noise reduction[35, 36]. Before imaging, SD rats were anesthetized with 7% chloral hydrate (350 mg kg^{-1}) by intraperitoneal injection and immobilized in the supine position. Intravesical administration of PBS, AuQCs (1.5 mM), or NADC (0.5 mM) was initiated via the urethra using a 20-gauge indwelling catheter needle. CT scans were acquired in the axial mode, and three-dimensional multiplanar reconstruction images were generated. CT numerical values in Hounsfield Units (HU) and corresponding standard deviations (SD) were retrieved from the average of three individual ROIs[37].

In vivo therapy in rat IC models using intravesical NADC

The therapeutic efficacies of intravesical NADC were evaluated in chronic, acute, and prophylactic IC rat models in six groups: healthy control, IC + PBS, IC + anti-NGF, IC + AuQCs, IC + DHODHi, and IC + NADC, where IC was induced by CYP. Non-invasive procedures for intravesical treatment were described as we reported[38]. In brief, a 20-gauge indwelling intravenous catheter was inserted into the bladder of rats through the urethra, and 0.5 mL of different agents was then instilled. For chronic IC, 50 mg kg^{-1} CYP was intraperitoneally administrated on days 1, 4, and 7, with intravesical therapy performed on days 8, 10, and 12. The AIC rat model was established using a high CYP dose of 150 mg kg^{-1} on day 1[14]. Therapeutic measures were conducted at 4 h and on day 3 post-injection. The prophylactic effect of NADC was estimated by intravesical drug administration to rat models on days 1, 3, and 5, followed by 150 mg kg^{-1} intraperitoneal CYP induction of cystitis on day 6. Therapeutic effects were assessed by conscious

cystometry and rodent Von Frey tests for bladder pain at the endpoint.

The Von Frey test

As the hallmark syndrome for IC, evoked bladder pain was assessed by the mechanical withdrawal responses with Von Frey filaments[39]. Rats were placed on a broad-gauge wire mesh surface and acclimatized to the chamber environment for 30 min before testing. Different calibrated Von Frey filaments with gradually increasing forces from a 1-g filament were administrated to the lower abdominal areas and poked onto the skin until minor bending was reached under the 50% withdrawal threshold technique. Withdrawal responses of rats, such as sudden retracting, lower abdomen licking, and jumping, were observed after reaching their threshold.

Conscious cystometry for bladder function testing

The bladder catheter was linked through a three-way stopcock to a BL-420N (information) biological signal acquisition and processing system (Chengdu Thai unita software) with a microinjection pump at the same height level as the bladder. Repeated bladder contractions were induced with 6 mL h^{-1} saline infusion at room temperature[40]. After an initial stabilization period of 30 min, the fluidic pressure and volume in the bladder were measured during cycles of filling, storage, and voiding, with a minimum of four cycles recorded. Data on intersystolic and maximal voiding pressures, voiding pressure threshold, and baseline resting pressure were derived from the curves.

Open field test

Abdominal pain has been shown to affect general activity levels, gross locomotor activity, and exploration behaviors, impacting patients' quality of life[41]. We employed sensorimotor OFT to study the influence of IC on rodent exploration footage. Rats with AIC receiving various treatments were placed in a clean chamber and allowed to move freely for a while, with an overhead video camera that covered the entire arena for recording. After that, the rat footage was recorded for 6 min at 30 frames s^{-1} (approximately 10,800 total frames) and analyzed using the Manual Tracking Manager plugin in ImageJ 1.8.0 (National Institutes of Health). The tail base of each rat in all frames was clicked and set to track the movement. Data were displayed in the rat's coordinates (X, Y) in each frame. The following formula is used to calculate the movement distance in each frame:

$$Distance = \sqrt{(x_2 - x_1)^2 + (y_2 - y_1)^2}$$

Where (x_1, y_1) dictates the position in the first frame and (x_2, y_2) represents the position in the second frame. The cumulative distance is quantified by adding the distance between each frame over a pre-defined period.

Macroscopic analysis of bladder gross pathology

Rats with IC were euthanized at pre-defined time points with bladders excised, weighed, and examined macroscopically for hemorrhage and edema. Bladder tissues were pathologically scored according to the following criteria: 3 points as severe (severe edema

of the bladder wall with significant bleeding), 2 points as moderate (moderate edema of the bladder wall with minor bleeding), 1 point as mild (minor edema with no bleeding), and 0 points as no effects[42, 43].

Histology

For histopathological examination, freshly resected bladder tissues were fixed in 4 % methanol-free paraformaldehyde, embedded in paraffin blocks, and sectioned into 8 μm in thickness. After staining by hematoxylin and eosin (H&E), the bladder sections were evaluated for the severity of inflammation according to the following grading criteria: 0 as normal, 1 as subepithelial inflammatory infiltration (focal and multifocal), 2 as edema and subepithelial inflammatory cell infiltration (diffuse), 3 as marked necrosis and neutrophils in and on the surface of the bladder mucosal epithelium with subepithelial inflammatory cells, 4 as inflammatory cell infiltration extending into muscles, and 5 as loss of superficial epithelial cells in addition to grade 3[44, 45].

Immunofluorescence analysis

We stained NGF with a labeled anti-NGF monoclonal antibody to track NADC in bladder mucosa and correlate with NGF expression. Typically, 130 nM CF488A in *N*-hydroxysuccinimide (NHS) ester (Biotium) was mixed with 2 μg anti-NGF antibodies in 1 mL PBS under stirring for 1 h at room temperature. Purification was achieved using a 3 kDa MWCO ultrafiltration tube with the retentate collected and stored at 4°C in the dark. After being anesthetized with 7% chloral hydrate, rats with CYP-induced cystitis were administered 0.5 mL AuQCs or NADC for 12 h by an intravesical catheter. Bladders were then isolated from rats, rinsed with PBS, and embedded in OCT for fresh cryosections. 8 μm thick sections were cut, blocked with 2% BSA for 1 h at room temperature, and stained with CF488A labeled anti-NGF antibodies (2 μg mL^{-1}) for 1 h at room temperature, with DAPI counterstaining (Beyotime)[46, 47]. After mounting, confocal imaging was performed using an LSM880 confocal laser scanning microscope (Zeiss) for colocalization analysis.

Western blot analyses

Harvested bladder tissues were homogenized in the lysis buffer (20∟mM HEPES–KOH, pH 7.5, 10∟mM KCl, 1.5∟mM $MgCl_2$, 0.2∟mM EDTA, 0.1% Triton-X100), with protein concentrations calibrated with a BCA kit (Pierce)[48]. 20 μg proteins were loaded onto sodium dodecyl-sulfate polyacrylamide gel electrophoresis (SDS-PAGE) gels and blotted onto polyvinylidene fluoride (PVDF) membranes[49]. After blocking, membranes were stained at 4 °C with the following primary antibodies at 1:1000 dilutions: tumor necrosis factor alpha (TNF-α, ab66579, Abcam), interleukin-1 beta (IL-1β, ab9722, Abcam), IL-6 (DF6087, Affinity Biosciences), NGF (ab52918, Abcam), IL-17A (ab79056, Abcam), tropomyosin receptor kinase A (TrkA, DF6822, Affinity Biosciences), phospho-TrkA (AF3072, Affinity Biosciences), nuclear factor kappa B (NF-κB, AF5006, Affinity Biosciences), phospho-NF-κB (AF2006, Affinity Biosciences), inhibitory-κB kinase alpha (IKK-α, AF6012, Affinity Biosciences), phospho-IKK-α (AF3012, Affinity Biosciences), IKK-β (AF6009, Affinity Biosciences), phospho-IKK-β (AF3010, Affinity Biosciences),

Janus kinase-1 (JAK-1, AF5012, Affinity Biosciences), phospho-JAK-1 (AF2012, Affinity Biosciences), signal transducer and activator of transcription 1 (STAT1, AF6300, Affinity Biosciences), phospho-STAT1 (AF3300, Affinity Biosciences), STAT2 (AF6342, Affinity Biosciences), phospho-STAT2 (AF3342, Affinity Biosciences), and β-actin (T0022, Affinity Biosciences). After further staining with goat anti-rabbit or goat anti-mouse matching secondary antibodies for 1 h, the blots were developed using Clarity ECL Western Blotting Substrate (Bio-Rad) for chemiluminescence. Band signals of proteins were analyzed with ImageJ.

mRNA sequencing

Bladder specimens were excised with autoclaved scissors, placed in a 5 mL sterile Eppendorf tube, and stored at -80 °C before sequencing. Paired-end sequencing reads of 2 x 150 bp in length were firstly trimmed and cleaned by fastp and aligned to *Rattus norvegicus* genome mRatBN7.2 (http://asia.ensembl.org/Rattus_norvegicus/Info/Index) by the HISAT2 aligner[50]. PCA was performed to identify similarities among samples and replicates. RNA-seq data were investigated for differentially expressed genes (DEGs) and gene set enrichment analysis (GSEA). The R package DESeq2 v1.38.3 was used to identify the significant DEGs with false discovery rate (FDR) < 0.001 and an absolute value of $\log_2$ ratio ≥ 2[51]. Gene annotations were downloaded from org.Rn.eg.db (Genome wide annotation for *Rattus noregicus* version 3.8.2.), and all ensemble gene IDs were mapped to symbol IDs using the R package AnnotationDbi v1.60.2 for further analysis[52]. Next, a universal GSEA was conducted using the R package clusterProfiler (gseKEGG function v 4.0.5), for which the DEG set pre-ranked by their log2 fold changes was compared with the KEGG pathway dataset as a reference to identify significantly enriched pathways in DEGs[53]. GO term enrichment analysis was conducted using g:Profiler portal (function g:GOSt ; https://biit.cs.ut.ee/gprofiler/gost). The association of genes and KEGG pathways was depicted as a network using the R package clusterProfile (function cnetplot v4.8.2)[54].

16S rRNA sequencing and metrics calculation

16S rRNA amplicon sequencing was performed using probes listed in Supplementary Table 2. Paired-end sequencing reads of 2 x 251 bp in length were pre-processed using the DADA2 v1.26.0 pipeline in R, including quality filtering and trimming, paired reads merging, and chimeras removing[55]. The number and percentage of reads that passed each step can be found in Supplementary Table 3. DADA2 was then used to assign the amplicon sequence variants (ASVs) to the processed reads, and taxonomy was assigned using the Silva database v138.1 to each sequence variant[56]. Raw sequencing data were archived under NCBI Bioproject PRJNA1085057, and codes for analyses are available at https://github.com/WanyanW/NADC-Microbiome-Yang. Richness (observed ASVs), Chao1, and ACE indexes were calculated to represent α diversity for each sample from rarefied sequence counts. Differences in the α-diversity index between any two groups were analyzed by the Wilcoxon test. β-Diversity metrics were calculated using the Bray-Curtis distance and represented by non-metric multidimensional scaling (NMDS) using the phyloseq R package v1.42.0[57]. ASVs with significant differences in abundance

between groups were evaluated by the linear discriminant analysis (LDA) effect size (LEfSe) method using the R package microbiomeMarker v1.4.0, and any ASVs with a *P* value < 0.05 and an LDA score (log10) > 2 were featured as microbiome biomarkers[58]. Linear regression modeling of the abundances of individual taxa against the treatment was conducted using the R package Microviz v0.11.0, and the results were plotted on the taxonomic tree generated from the taxonomic table[59]. The regression coefficient estimates, test statistics, and corresponding *P* values from all these regression models can be found in Supplementary Table 4.

Data availability

The data supporting the work's findings are deposited and available in the public medical database, *Research Data Deposit* (RDD), with the designated identifier # (to be assigned upon gallery proof).

Acknowledgments

We thank Agropur for providing the high-purity α-LA for synthesis. The authors further acknowledge the National Natural Science Foundation of China (82071978 and 52271196) and the National Key Research and Development Program of China (2021YFF1200700) for supporting the study.

Author contributions

J.Y. and Z.L. conceived and designed the study. Z.L., W.W., and D.L. conducted experiments and collected, managed, and visualized the data. W.W. performed bioinformatic analyses, coding, and visualization with technical help and advice from Q.Z. and Y.S. Further, Z.L. and Z.X. jointly performed spectral CT imaging, and Y.H. and X.Z assisted urodynamic analyses. Z.W. helped with human tissue collection and analysis. J.Y. supervised the project. X.Z. provided resources and technical advice for the project. J.Y. and Z.L. co-wrote the manuscript, which was revised, proofread, and approved by all authors.

Competing interests

The authors filed a pending patent application related to the work.

References

1. Garzon S*, et al.* An update on treatment options for interstitial cystitis. *Prz Menopauzalny* **19**, 35-43 (2020).
2. Lin Z*, et al.* Biomaterial-assisted drug delivery for interstitial cystitis/bladder pain syndrome treatment. *J Mater Chem B* **9**, 23-34 (2021).
3. Abreu-Mendes P, Pinto R, Oliveira PD. Systemic therapy for bladder pain syndrome/interstitial cystitis (BPS/IC): systematic review of published trials in the last 5 years. *Curr Bladder Dysfunct Rep* **15**, 192-202 (2020).
4. Kuo HC. Intravesical injections of autologous platelet-rich plasma for the treatment of refractory interstitial cystitis. *Low Urin Tract Symptoms* **15**, 210-215 (2023).
5. Mostafa MM, Kamel M, Kamel M, Mahdy A. Interstitial Cystitis/Bladder Pain Syndrome:

Role of Bladder Inflammation in Bladder Function. *Curr Bladder Dysfunct Rep* **19**, 16-26 (2024).

6. Bannwarth B, Kostine M. Nerve growth factor antagonists: is the future of monoclonal antibodies becoming clearer? *Drugs* **77**, 1377-1387 (2017).
7. Fox R, Wiendl H, De Stefano N, Sellner J, Muehler A. Efficacy and safety of the selective oral DHODH modulator vidofludimus calcium (IMU-838) in relapsing multiple sclerosis (EMPhASIS): a randomized, placebo-controlled phase 2 trial. *Neurology* **96**, (2021).
8. Zhang W, Liu X, Wang J, Wang X, Zhang Y. Immunogenic Cell Death Associated Molecular Patterns and the Dual Role of IL17RA in Interstitial Cystitis/Bladder Pain Syndrome. *Biomolecules* **13**, 421 (2023).
9. D'Cunha R*, et al.* A first-in-human study of the novel immunology antibody-drug conjugate, ABBV-3373, in healthy participants. *Br J Clin Pharmacol* **90**, 189-199 (2024).
10. Wang H, Chen D, Lu H. Anti-bacterial monoclonal antibodies: next generation therapy against superbugs. *Appl Microbiol Biotechnol* **106**, 3957-3972 (2022).
11. Zhao CH*, et al.* Near-Infrared Phototheranostic Iron Pyrite Nanocrystals Simultaneously Induce Dual Cell Death Pathways via Enhanced Fenton Reactions in Triple-Negative Breast Cancer. *ACS Nano* **17**, 4261-4278 (2023).
12. Firer MA, Luboshits G. Antibody-Drug-Conjugate Therapy for Hematological Cancers: Matching Cell Biology with Clinical Benefit. *Adv Funct Mater* **31**, 2100032 (2021).
13. Akiyama Y. Biomarkers in Interstitial Cystitis/Bladder Pain Syndrome with and without Hunner Lesion: A Review and Future Perspectives. *Diagnostics* **11**, 2238 (2021).
14. Dayem AA, Kim K, Lee SB, Kim A, Cho SG. Application of Adult and Pluripotent Stem Cells in Interstitial Cystitis/Bladder Pain Syndrome Therapy: Methods and Perspectives. *J Clin Med* **9**, 766 (2020).
15. Ding J*, et al.* Aptamer-modified atomically precise gold nanoclusters as targeted nanozymes to scavenge reactive oxygen species in white adipocytes. *Nanotechnology* **34**, 365101 (2023).
16. Bai Y, Li H, Lv R. Interleukin-17 activates JAK2/STAT3, PI3K/Akt and nuclear factor-kappaB signaling pathway to promote the tumorigenesis of cervical cancer. *Exp Ther Med* **22**, 1291 (2021).
17. Oledzka AJ, Czerwinska ME. Role of Plant-Derived Compounds in the Molecular Pathways Related to Inflammation. *Int J Mol Sci* **24**, 4666 (2023).
18. Xu H*, et al.* Combined Signature of the Urinary Microbiome and Metabolome in Patients With Interstitial Cystitis. *Front Cell Infect Microbiol* **11**, 711746 (2021).
19. Mutreja I, Maalej N, Kaushik A, Kumar D, Raja A. High atomic number nanoparticles to enhance spectral CT imaging aspects. *Mater Adv* **4**, 3967-3988 (2023).
20. Kovtun YV*, et al.* Antibody-drug conjugates designed to eradicate tumors with homogeneous and heterogeneous expression of the target antigen. *Cancer Res* **66**, 3214-3221 (2006).
21. Zhang CO, Wang JY, Koch KR, Keay S. Regulation of tight junction proteins and bladder epithelial paracellular permeability by an antiproliferative factor from patients with interstitial cystitis. *J Urol* **174**, 2382-2387 (2005).

22. Beishenaliev A, *et al.* Bispecific antibodies for targeted delivery of anti-cancer therapeutic agents: A review. *J Control Release* **359**, 268-286 (2023).
23. Liu T, *et al.* The IL-23/IL-17 Pathway in Inflammatory Skin Diseases: From Bench to Bedside. *Front Immunol* **11**, 594735 (2020).
24. Lopez L, *et al.* The response to TNF blockers depending on their comparator in rheumatoid arthritis clinical trials: the lessebo effect, a meta-analysis. *Rheumatology (Oxford)* **61**, 531-541 (2022).
25. Braga RM, Dourado MN, Araujo WL. Microbial interactions: ecology in a molecular perspective. *Braz J Microbiol* **47**, 86-98 (2016).
26. Blander JM, Longman RS, Iliev ID, Sonnenberg GF, Artis D. Regulation of inflammation by microbiota interactions with the host. *Nat Immunol* **18**, 851-860 (2017).
27. Yang J, *et al.* Gold/alpha-lactalbumin nanoprobes for the imaging and treatment of breast cancer. *Nat Biomed Eng* **4**, 686-703 (2020).
28. Song Y-T, *et al.* Application of antibody-conjugated small intestine submucosa to capture urine-derived stem cells for bladder repair in a rabbit model. *Bioactive Materials* **14**, 443-455 (2022).
29. Kim S, *et al.* Antigen-Antibody Interaction-Derived Bioadhesion of Bacterial Cellulose Nanofibers to Promote Topical Wound Healing. *Adv Funct Mater* **32**, 2110557 (2022).
30. Zhang H, *et al.* APOE interacts with ACE2 inhibiting SARS-CoV-2 cellular entry and inflammation in COVID-19 patients. *Signal Transduction Targeted Therapy* **7**, 261 (2022).
31. Kavand H, Nasiri R, Herland A. Advanced materials and sensors for microphysiological systems: focus on electronic and electrooptical interfaces. *Advanced Materials* **34**, 2107876 (2022).
32. Li G, *et al.* Collagen-targeted tumor-specific transepithelial penetration enhancer mediated intravesical chemoimmunotherapy for non-muscle-invasive bladder cancer. *Biomaterials* **283**, 121422 (2022).
33. Lin ZJ, *et al.* A near-infrared fluorescence-enhancing plasmonic biosensing microarray identifies soluble PD-L1 and ICAM-1 as predictive checkpoint biomarkers for cancer immunotherapy. *Biosens Bioelectron* **240**, 115633 (2023).
34. Chen J, *et al.* A H_2O_2-activatable nanoprobe for diagnosing interstitial cystitis and liver ischemia-reperfusion injury via multispectral optoacoustic tomography and NIR-II fluorescent imaging. *Nat Commun* **12**, 6870 (2021).
35. Galluzzo A, Danti G, Bicci E, Mastrorosato M, Bertelli E, Miele V. The Role of Dual-Energy CT in the Study of Urinary Tract Tumors: Review of Recent Literature. *Semin Ultrasound CT MRI* **44**, 136-144 (2023).
36. Lu XK, *et al.* 3D microstructure design of lithium-ion battery electrodes assisted by X-ray nano-computed tomography and modelling. *Nat Commun* **11**, 2079 (2020).
37. Liu DX, *et al.* Selective Organ-Targeting Hafnium Oxide Nanoparticles with Multienzyme-Mimetic Activities Attenuate Radiation-Induced Tissue Damage. *Advanced Materials*, 2308098 (2024).
38. Lin ZJ, *et al.* Nanoparticle-mediated intravesical delivery of conditioned medium derived from mesenchymal stem cells for interstitial cystitis/bladder pain syndrome

treatment. *Appl Mater Today* **24**, 101144 (2021).

39. Chen JL*, et al.* Normalization of magnesium deficiency attenuated mechanical allodynia, depressive-like behaviors, and memory deficits associated with cyclophosphamide-induced cystitis by inhibiting TNF-alpha/NF-kappaB signaling in female rats. *J Neuroinflammation* **17**, 99 (2020).
40. Hao F*, et al.* Proper wiring of newborn neurons to control bladder function after complete spinal cord injury. *Biomaterials* **292**, 121919 (2023).
41. Fu H*, et al.* Associations between disease activity, social support and health-related quality of life in patients with inflammatory bowel diseases: the mediating role of psychological symptoms. *BMC Gastroenterol* **20**, 11 (2020).
42. Augé C, Gamé X, Vergnolle N, Lluel P, Chabot S. Characterization and Validation of a Chronic Model of Cyclophosphamide-Induced Interstitial Cystitis/Bladder Pain Syndrome in Rats. *Front Pharmacol* **11**, 1305 (2020).
43. Wang X*, et al.* Shionone alleviates NLRP3 inflammasome mediated pyroptosis in interstitial cystitis injury. *International Immunopharmacology* **90**, 107132 (2021).
44. Wang Z*, et al.* Exosomes derived from bladder epithelial cells infected with uropathogenic Escherichia coli increase the severity of urinary tract infections (UTIs) by impairing macrophage function. *PLoS Pathog* **20**, e1011926 (2024).
45. D'Amico R*, et al.* Hidrox® and Chronic Cystitis: Biochemical Evaluation of Inflammation, Oxidative Stress, and Pain. *Antioxidants* **10**, 1046 (2021).
46. Lin SH, Huang APH, Hsu SH. Injectable, Micellar Chitosan Self-Healing Hydrogel for Asynchronous Dual-Drug Delivery to Treat Stroke Rats. *Adv Funct Mater* **33**, 2303853 (2023).
47. Zhu Z*, et al.* An Enzyme - Activatable Aggregation - Induced - Emission Probe: Intraoperative Pathological Fluorescent Diagnosis of Pancreatic Cancer via Specific Cathepsin E. *Advanced Materials* **34**, 2107444 (2022).
48. Sun Z*, et al.* Multi-omics approaches revealed the therapeutic mechanisms of Suo-Quan-Wan for treating overactive bladder in spontaneously hypertensive rats. *Journal of Ethnopharmacology* **318**, 117066 (2024).
49. Xing Y, Yerneni SS, Wang W, Taylor RE, Campbell PG, Ren X. Engineering pro-angiogenic biomaterials via chemoselective extracellular vesicle immobilization. *Biomaterials* **281**, 121357 (2022).
50. Kim D, Paggi JM, Park C, Bennett C, Salzberg SL. Graph-based genome alignment and genotyping with HISAT2 and HISAT-genotype. *Nat Biotechnol* **37**, 907-915 (2019).
51. Love MI, Huber W, Anders S. Moderated estimation of fold change and dispersion for RNA-seq data with DESeq2. *Genome Biol* **15**, 550 (2014).
52. Pagès H, Carlson M, Falcon S, Li N. AnnotationDbi: manipulation of SQLite-based annotations in bioconductor. R package version 1.62. 2. *Bioconductor*, (2023).
53. Wu T*, et al.* clusterProfiler 4.0: A universal enrichment tool for interpreting omics data. *Innovation (Camb)* **2**, 100141 (2021).
54. Yu G, Wang LG, Han Y, He QY. clusterProfiler: an R package for comparing biological

themes among gene clusters. *Omics* **16**, 284-287 (2012).

55. Callahan BJ, McMurdie PJ, Rosen MJ, Han AW, Johnson AJ, Holmes SP. DADA2: High-resolution sample inference from Illumina amplicon data. *Nat Methods* **13**, 581-583 (2016).
56. Quast C*, et al.* The SILVA ribosomal RNA gene database project: improved data processing and web-based tools. *Nucleic Acids Res* **41**, D590-596 (2013).
57. McMurdie PJ, Holmes S. phyloseq: an R package for reproducible interactive analysis and graphics of microbiome census data. *PLoS One* **8**, e61217 (2013).
58. Cao Y, Dong Q, Wang D, Zhang P, Liu Y, Niu C. microbiomeMarker: an R/Bioconductor package for microbiome marker identification and visualization. *Bioinformatics* **38**, 4027-4029 (2022).
59. Barnett DJ, Arts IC, Penders J. microViz: an R package for microbiome data visualization and statistics. *Journal of Open Source Software* **6**, 3201 (2021).

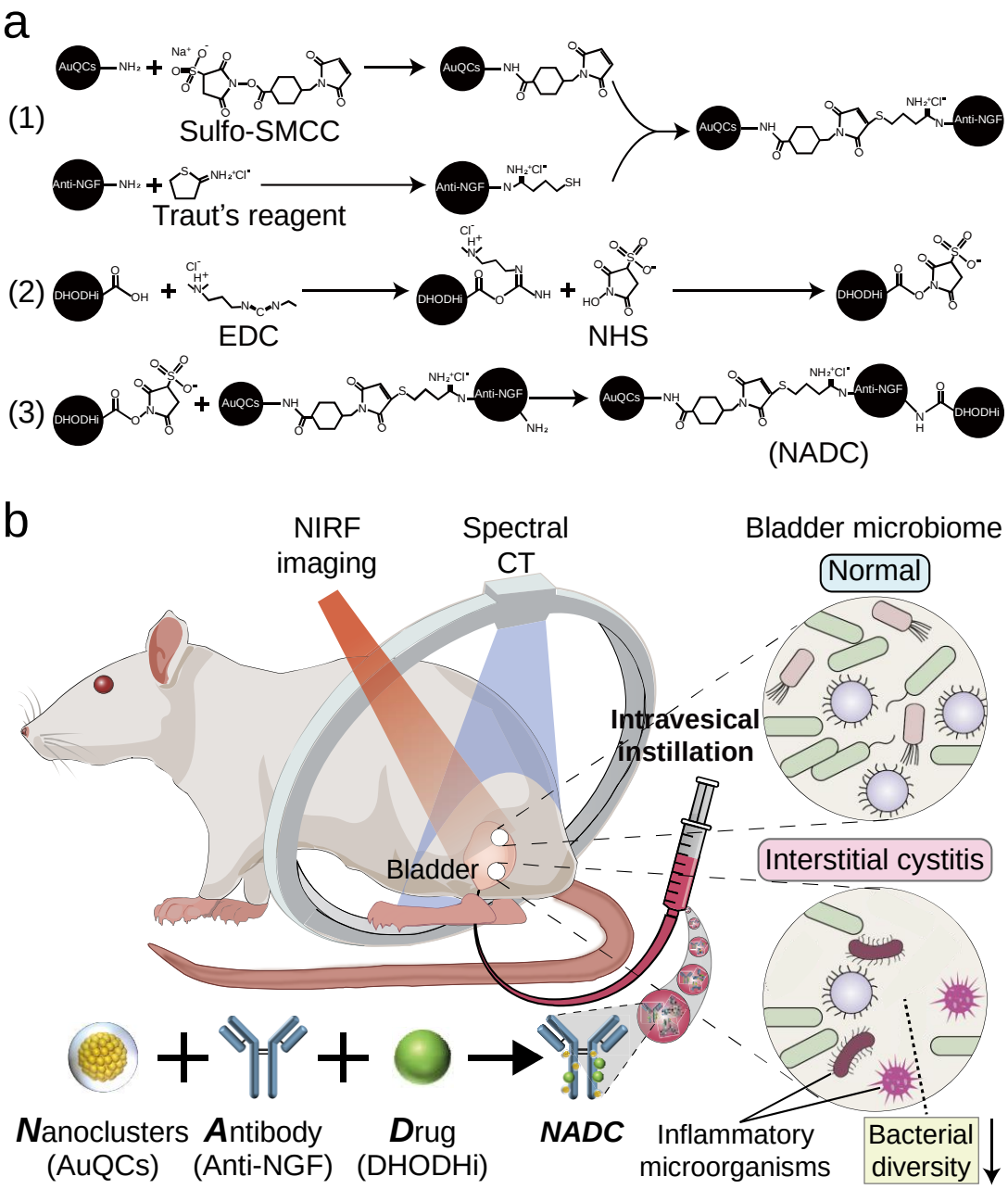

Figure 1. Synthesis pathways of NADC and concept of intravesical theranostic NADC against interstitial cystitis (IC). (a) Schematic diagram of the synthesis process of NADC. (1) Solvent-accessible primary amino groups of AuQCs react with the sulfo-N-hydroxysuccinimide (NHS) ester of the sulfosuccinimidyl 4-(N-maleimidomethyl) cyclohexane-1-carboxylate (sulfo-SMCC) crosslinker to acquire maleimide-terminated derivatives reactive towards sulfhydryls. Concurrently, primary amines from the lysine side chains of the anti-NGF tanezumab antibody react with the cyclic thioimidate compound, Traut's Reagent (2-iminothiolane), to introduce a reactive sulfhydryl group in one step that is successively crosslinked to maleimide-activated AuQCs. (2) The benzoic acid group of the dihydroorotate dehydrogenase inhibitor (DHODHi), vidofludimus, is activated by 1-ethyl-3-(3-dimethyl aminopropyl) carbodiimide (EDC) to form the O-acylisourea ester intermediate, which is in turn

stabilized by sulfo-NHS to derive the amine-reactive DHODHi molecule. (3) The remaining unreacted amines on tanezumab are covalently crosslinked with the DHODHi NHS ester to yield the final NADC product. (b) Theranostic AuQCs and an immunosuppressive DHODHi, vidofludimus, are conjugated through covalent linkage to a humanized NGF antagonistic monoclonal IgG2 antibody, tanezumab, which targets elevated NGF in response to bladder inflammation. The therapeutic efficacy of NADC is synergized from the combination of AuQCs, vidofludimus, and tanezumab, encompassing concomitant regulation of multiple inflammation-associated signaling pathways and remodeling of the host bladder microbiota. Intravesically instilled NADC allows bilateral management of IC through simultaneously alleviating inflammation and pain, image-guided by dual-modality NIRF and CT.

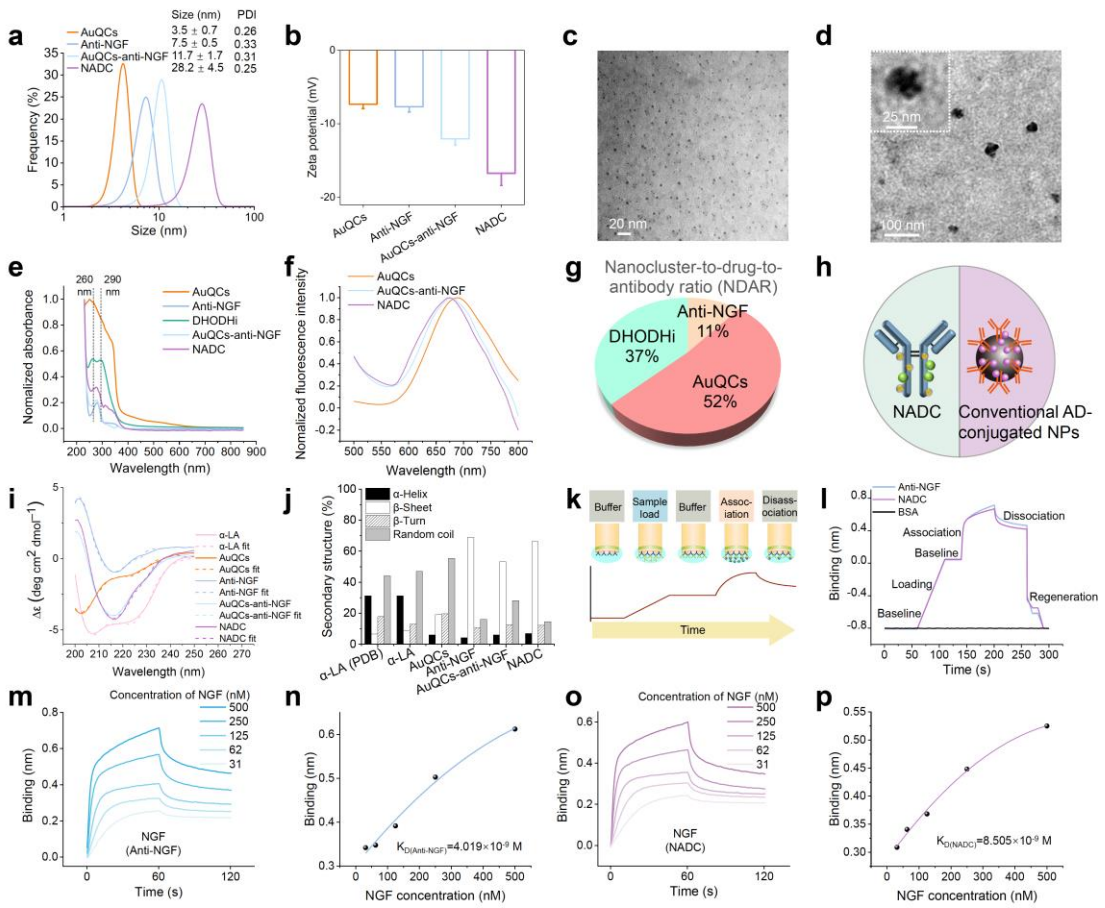

Figure 2. Characterization of NADC. (a) DLS analysis for the hydrodynamic size distribution and (b) zeta potential of NADC and its individual constituents. Representative TEM images of (c) ultrasmall-sized AuQCs (<3 nm) and (d) NADC (~ 25 nm). (e) Normalized UV-vis absorption spectra showing distinct feature peaks of DHODHi at 260 and 290 nm (dotted lines) and a broadened peak at 280 nm of tanezumab in NADC. (f) Normalized fluorescence emission spectra of NADC at the excitation wavelength of 360 nm. A minor hypsochromic shift in the NIRF emission peak of AuQCs was observed upon covalent interaction with tanezumab. (g) The molar NDAR of each constituent in NADC. (h) A schematic comparison between NADC in this study and conventional antibody-drug-conjugated NPs. (i) Far-UV CD spectra of NADC and individual constituents. The dotted lines indicate fitted curves by applying the BeStSel algorithm to data for secondary structure determination and folding recognition. (j) Calculated secondary structure compositions of NADC, with its structural components predominantly contributed by the anti-NGF antibody as the framework. The structure of apo-state bovine α-LA retrieved from RSCB (Protein Data Bank ID: 1F6R) was quantified in consistency with experimental data. (k) Schematic representation of BLI sensorgrams showing the interferometric binding signal change with assay processes. (l) BLI sensorgrams showing the loading, binding, association, and disassociation steps of anti-NGF antibody and NADC, with BSA as a control. Tanezumab and NADC were successfully immobilized on the AHC biosensor surface by anti-human IgG Fc captures in similar binding kinetics. Real-time binding kinetics of

the anti-NGF antibody (m and n) and NADC (o and p) were monitored by BLI for association and dissociation to probe interactions with gradient concentrations of recombinant NGF at a 2-fold increment. Steady-state analyses (n and p) were performed for K_D determination. NADC retained the high binding affinity of tanezumab at the same order of magnitude at nanomolar levels.

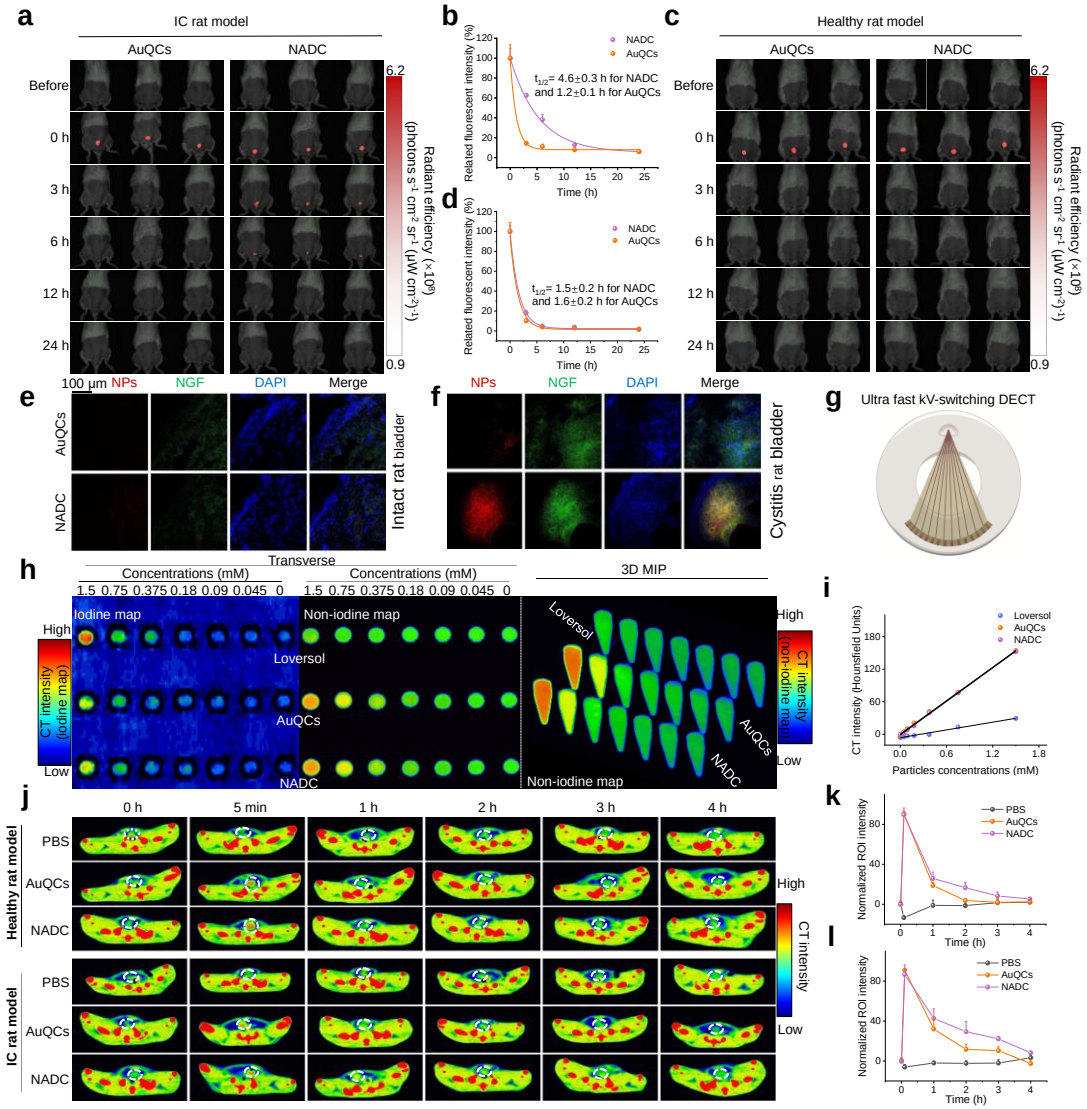

Figure 3. NADC as a dual-modality contrast agent for imaging IC. Time-course in vivo NIRF imaging of (a, b) rats with CYP-induced cystitis and (c, d) in healthy conditions after intravesical administration of AuQCs or NADC. In IC rats, the bladder clearance of NADC was distinctly more belated than that of AuQCs, resulting from its larger bladder retention half-life ($t_{1/2}$= 4.6 ± 0.3 h, R^2=0.996). In contrast, no difference in bladder retention and clearance between AuQCs ($t_{1/2}$= 1.6 ± 0.2 h, R^2=0.943) and NADC ($t_{1/2}$= 1.5 ± 0.2 h, R^2=0.965) was perceived in healthy rats, indicating rapid urinary excretion without potentially causing systemic toxicity. (e, f) Immunofluorescence of bladder tissue sections harvested from healthy and cystitis rats by confocal laser scanning microscopy (CLSM). CLSM images of bladder tissues from intact healthy (e) and IC rats (f) after intravesical instillation of AuQCs or NADC. NGF in healthy rat bladder displayed limited expression levels but is upregulated after the development of IC, as indicated by the strong fluorescence (green). Although AuQCs were enriched in the inflammation sites to some extent in the bladder of IC rats, targeting NADC displayed stronger NIR fluorescence (red) in high-degree co-localization with NGF. More importantly, minimal NADC was observed in healthy

bladder sections, verifying the effective in vivo IC targeting that would impose minimized in vivo toxicity with low body retention. (g) A schematic diagram showing the setup of a dual-energy CT scanner. (h) Spectral CT phantom images of loversol, AuQCs, and NADC at gradient concentrations. (i) The correlation between the concentration of contrast agents and the CT signal intensity. (j) Planar spectral CT images of the bladder at various time points after intravesical administration of indicated agents to healthy rats or rats with IC. Corresponding calculated intensities for the bladder ROIs (white dotted circles) of (k) healthy rats and (l) rats with IC.

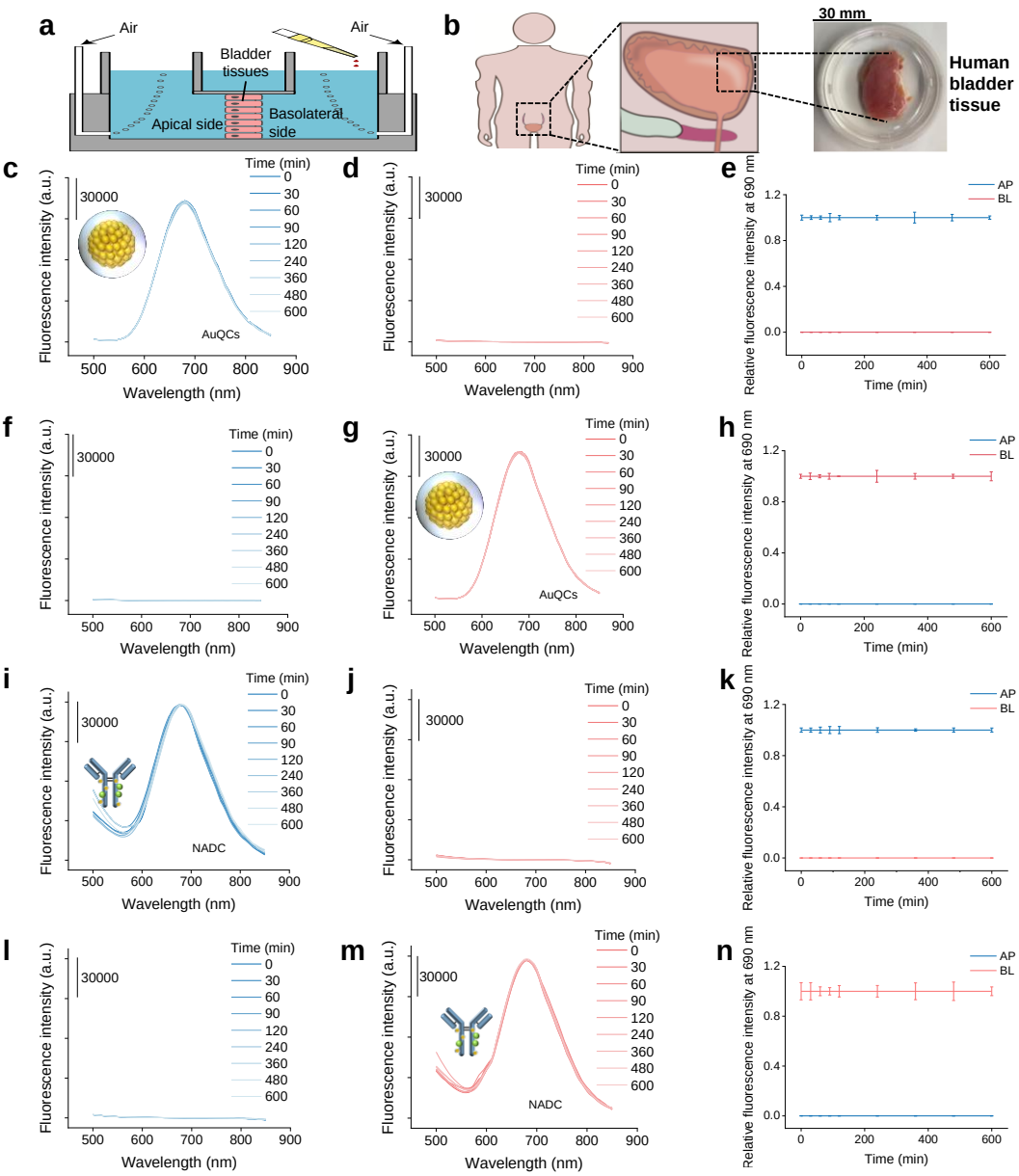

Figure 4. Evaluation of mucosal drug transport of NADC across human bladder tissues by Ussing chamber tests. (a) A schematic illustration of the Ussing chamber test using human bladder tissues. The chamber was perfused with gas, and NADC was introduced on one side of the chamber. By sampling from both sides of the chamber at specified intervals, we assessed the transcellular and paracellular transports. (b) A photograph of a human bladder tissue piece surgically resected from a patient. (c-h) AuQCs were added to (c-e) the apical (AP) side (blue) or (f-h) the basolateral (BL) side (red), with samples collected at predetermined intervals to measure fluorescence spectra on both sides. Fluorescence spectra on (c, f) the AP side and (d, g) the BL side. (e, h) NIRF intensities on both sides as a function of time. (i-n) Similarly, NADC was introduced to either (i-k) the AP side or (l-n) the BL side. Fluorescence spectra on (i, l) the AP side and (j, m) the BL side. (k, n) NIRF intensities on both sides as a function of time.

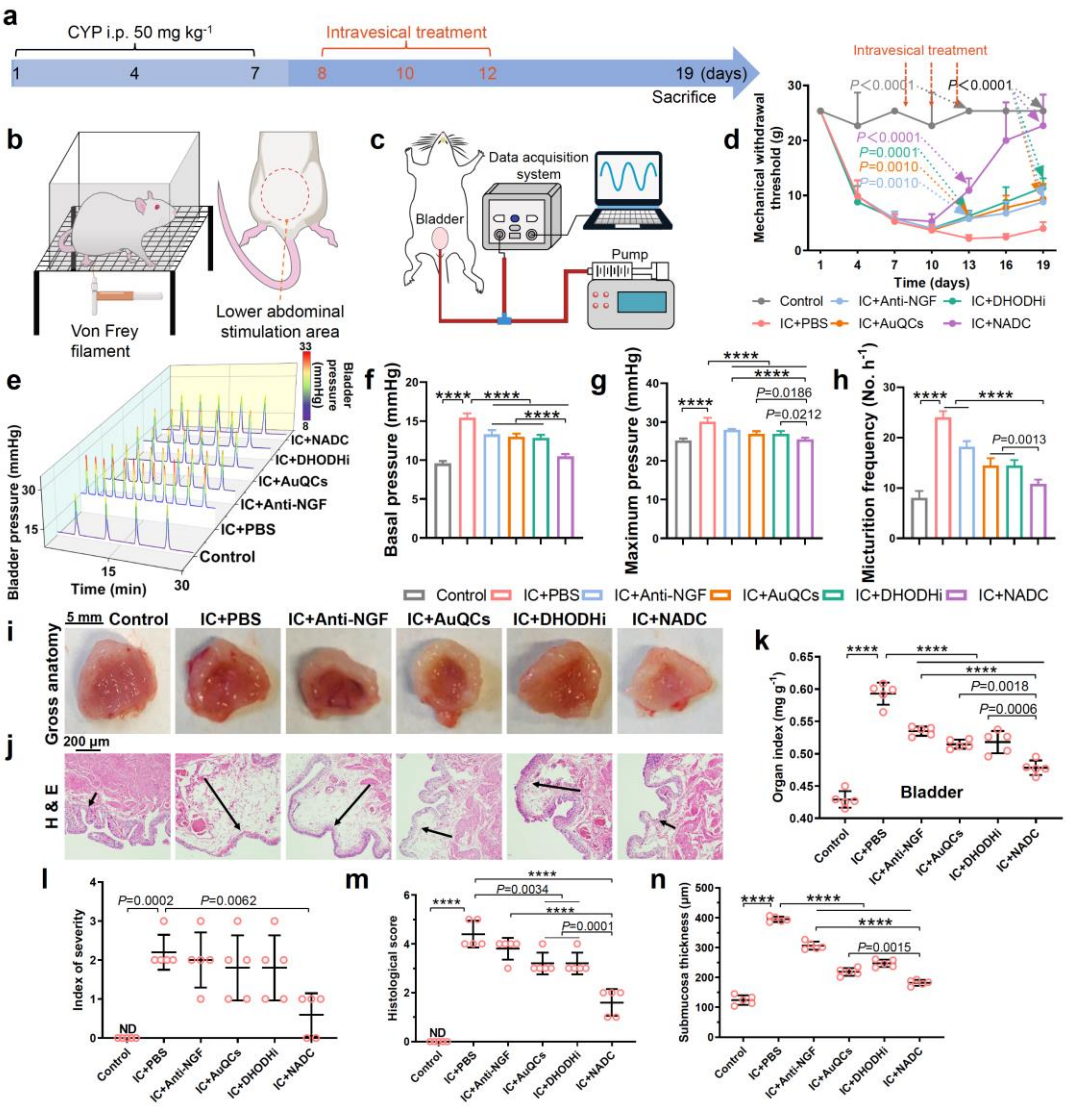

Figure 5. NADC as a therapeutic agent to treat chronic IC in rats. (a) Flowchart showing the chronic IC induction and therapeutic regimens in rats. Schematic illustrations of the procedures for (b) the Von Frey filament test and (c) urodynamics. (d) Changes in the mechanical allodynia threshold over time in chronic IC rat models receiving indicated interventions. All statistical analyses between groups in *P* values were made by comparison with the IC+PBS group. (e) Real-time bladder urodynamic curves of rats with chronic IC in different groups. (f) The basal pressure, (g) maximum pressure, and (h) micturition frequency of bladder urodynamics in different rat groups. (i) Gross anatomy of rat bladders harvested at the therapeutic endpoint of intravesical infusion. NADC significantly reduced symptoms of IC-induced congestion, bleeding, and edema. (j) Histopathology of resected bladders in indicated treatment groups by H&E staining. The length of the arrow indicates the bladder's mucosal edema zone. (k) Bladder organ index defined by the bladder weight/body weight ratio, (l) index of severity, (m) histological scores, and (n) submucosa thickness. Statistical significance levels: ****$P \leq 0.0001$.

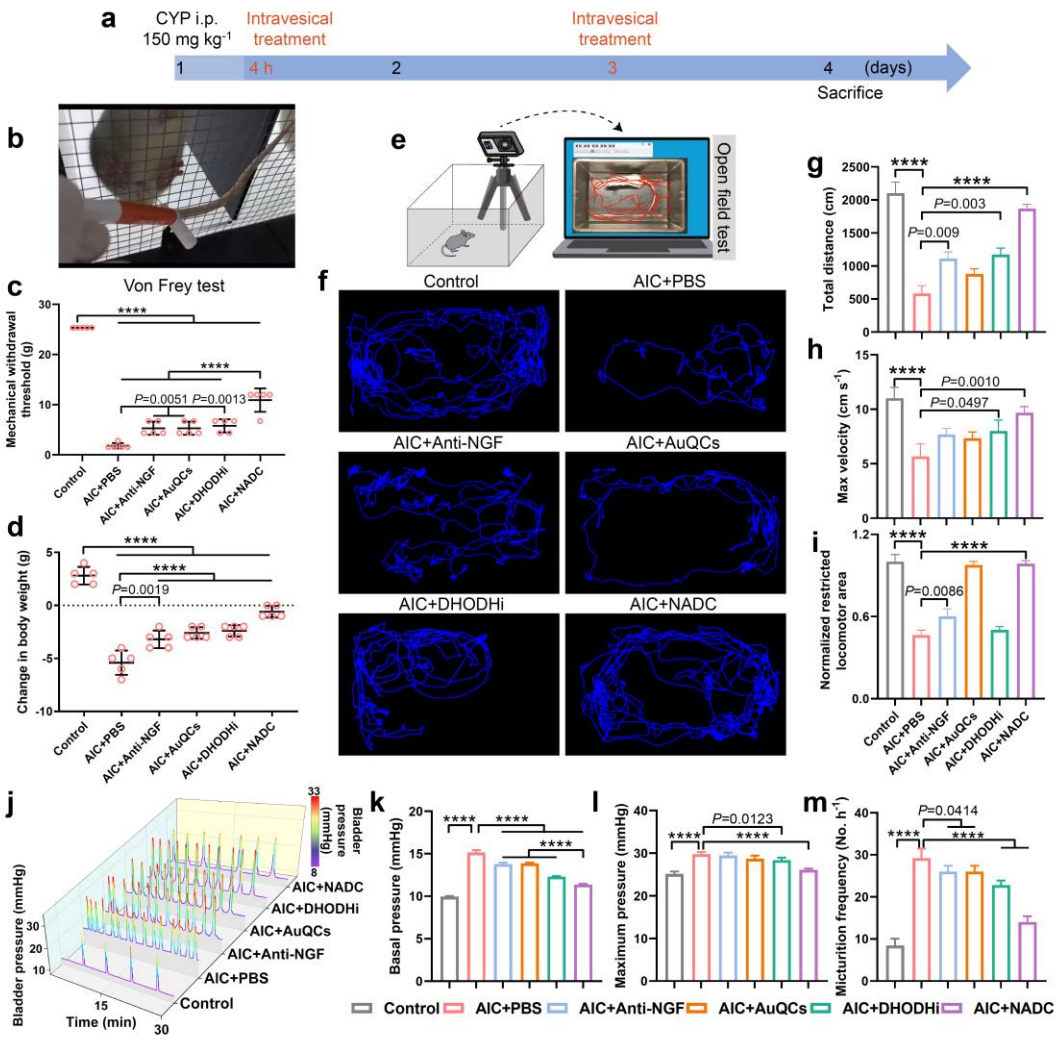

Figure 6. NADC as a therapeutic agent to treat AIC in rats. (a) Flowchart showing the AIC induction and therapeutic regimens in rats. (b) Representative photograph of the Von Frey filament test in a rat with AIC. (c) Mechanical withdrawal thresholds of rats receiving indicated intravesical interventions. (d) Body weight changes of rats after treatment at the study endpoint. (e) Schematic illustration showing the setup of open field tests (OFT) in the study. (f) Travel trajectories of the exploration footage of rats with AIC receiving various treatments. (g) The corresponding total traveled distance, (h) maximum velocity, and (i) normalized restricted locomotor area of rats from different groups. (j) Real-time bladder urodynamic curves of rats with AIC in different groups. (k) The basal pressure, (l) maximum pressure, and (m) micturition frequency of bladder urodynamics in different rat groups. Statistical significance levels: ****$P \leq 0.0001$.

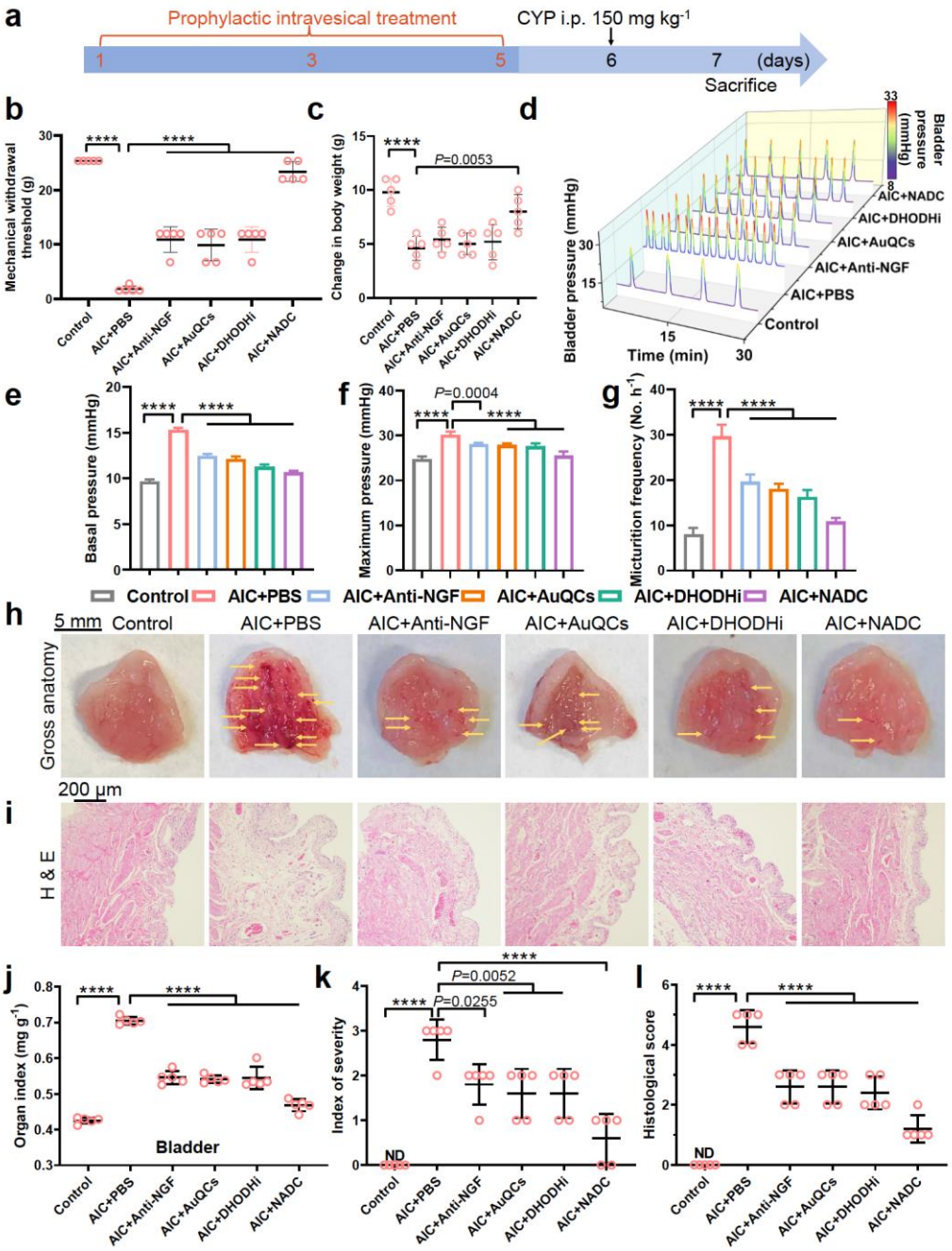

Figure 7. NADC as a prophylactic agent for AIC in rats. (a) Flowchart showing the therapeutic regimens of rats followed by AIC induction. (b) Mechanical withdrawal thresholds of rats receiving indicated intravesical prophylaxis before AIC induction. (c) Body weight changes of AIC rats receiving prophylactic treatment at the study endpoint. (d) Real-time bladder urodynamic curves of AIC rats with prophylactic treatment. (e) The basal pressure, (f) maximum pressure, and (g) micturition frequency of bladder urodynamics in AIC rats receiving pre-administration of intravesical prophylaxis. (h) Gross anatomy of bladders harvested from rats receiving intravesical prophylaxis before AIC induction. Yellow arrows indicate bleeding lesions in bladder tissues. (i) Histopathology of resected bladders in AIC rats with pre-administered prophylactic treatment by H&E staining. (j) Bladder organ index, (k) index of severity, and (l) histological scores. Statistical significance levels: ****$P \leq 0.0001$.

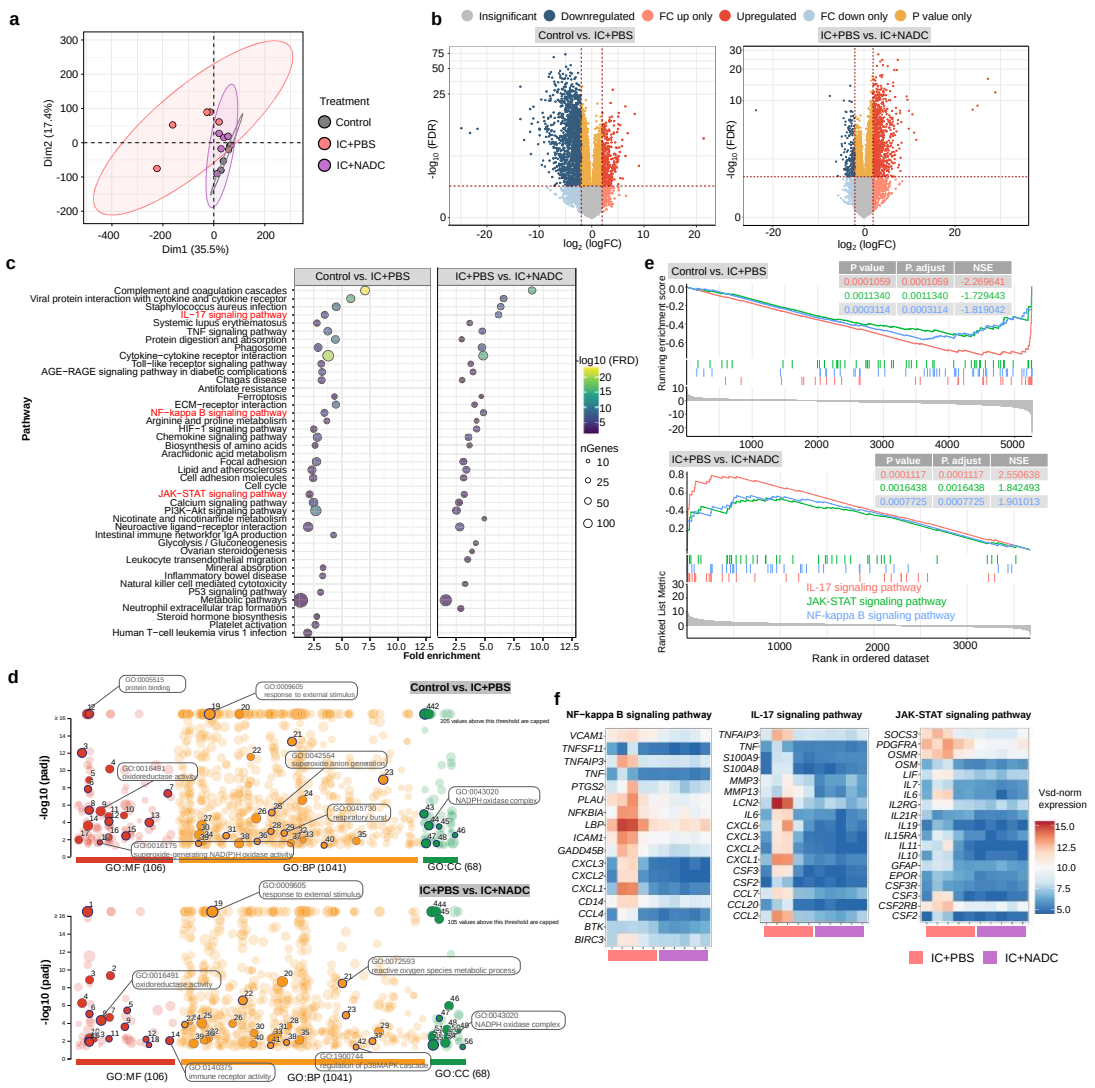

Figure 8. Coordinative molecular mechanisms of NADC. (a) PCA of the RNA-seq raw data indicates that IC is the primary factor distinguishing sample populations. Dim1 and Dim2 represent the first and second dimensions, respectively. (b) Volcano plots illustrate the pattern distribution of DEGs between compared groups by RNA-seq. An elevated number of DEGs are altered by IC in both upregulated and downregulated categories but are substantially reverted following intravesical NADC instillation. (c) KEGG pathways derived from DEGs post-NADC treatment with low and high q-values denoted in blue and green. The circle size reflects enriched gene counts. (d) GO enrichment mapping that is specifically relevant to IC occurrence and follow-up intravesical NADC. (e) GSEA of intravesical NADC therapy predominantly correlated with the NF-κB, IL-17, and JAK-STAT signaling pathways. (f) Heatmaps of significantly altered key effector genes in the NF-κB, IL-17, and JAK-STAT pathways in IC rat bladder tissues with or without NADC treatment. Expression values from high to low are displayed in color gradients ranging from red to blue.

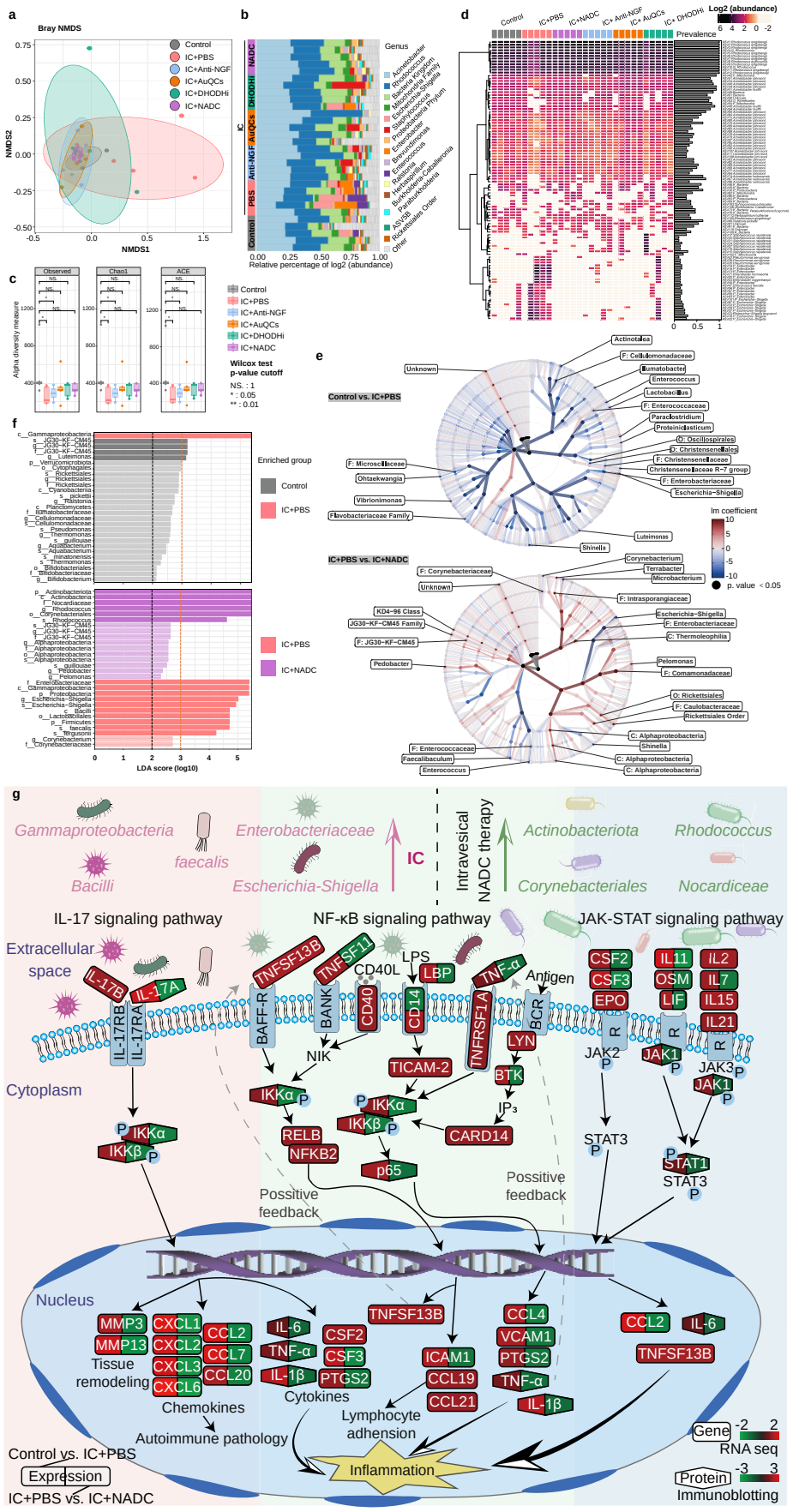
a
Bray NMDS
Control
IC+PBS
IC+Anti-NGF
IC+AuQCs
IC+DHODHi
IC+NADC
NMDS1
NMDS2
b
Genus
Relative percentage of log2 (abundance)
c
Observed
Chao1
ACE
Alpha diversity measure
Wilcox test
p-value cutoff
NS. : 1
* : 0.05
** : 0.01
d
Log2 (abundance)
Prevalence
e
Control vs. IC+PBS
IC+PBS vs. IC+NADC
lm coefficient
p. value < 0.05
f
Enriched group
Control
IC+PBS
IC+NADC
LDA score (log10)
g
Gammaproteobacteria
faecalis
Bacilli
Enterobacteriaceae
Escherichia-Shigella
IC
Intravesical NADC therapy
Actinobacteriota
Rhodococcus
Corynebacteriales
Nocardiceae
IL-17 signaling pathway
NF-κB signaling pathway
JAK-STAT signaling pathway
Extracellular space
Cytoplasm
Nucleus
Possitive feedback
Tissue remodeling
Chemokines
Cytokines
Lymphocyte adhension
Autoimmune pathology
Inflammation
Control vs. IC+PBS
Expression
IC+PBS vs. IC+NADC
Gene
RNA seq
Protein
Immunoblotting

Figure 9. Alleviation of IC through bladder microbiota modulation by NADC. (a) NMDS analysis of Bray-Curtis distances across bladder tissue samples revealed distinct microbiota compositions in IC-afflicted rats, markedly divergent from those in other treatment cohorts. Each point symbolizes the bladder microbiota of an individual rat, with the NMDS data highlighting significant microbial distinctions. (b) A bar graph illustrated the genus-level relative abundance of gut microbiota. (c) Variations in alpha diversity among different groups were presented, including observed counts, species richness (Chao1), the ACE, Shannon and Simpson index. The alpha diversity in the bladder microbiome of the IC+PBS group is notably lower, a condition that NADC treatment manages to improve partially. Statistical significance is denoted by * ($p < 0.05$) and ** ($p < 0.001$), as determined by Wilcoxon rank sum tests. (d) A heatmap displayed the relative abundance (above a 0.001 cutoff) and prevalence (above a 75% cutoff) of prokaryotic OTUs in the examined bladder tissue samples. (e) A clade diagram illustrated the phylogenetic distribution of microbial lineages pertinent to these two groups, with each smaller circle representing a taxonomic level‘s taxon and its diameter corresponding to relative abundance (the layers from the inner to the outer ring represent genus, family, order, class, and phylum, respectively). (f) Statistical analyses employing the LDA effect size method revealed significant taxa between groups, identified by an alpha value of 0.05 and an LDA (log10) absolute value greater than 2.0. The Gammaproteobacteria class and the JG30-KF-CM45 lineage (from family to species) were found to be significantly more abundant in IC, as indicated by LDA scores ≥3.0 using LEfSe, implicating them in disease pathogenesis. (g) Mechanistic synergy of intravesical NADC therapy against IC by coordinating NF-κB, IL-17, and JAK-STAT signal transduction pathways. Effectors in mRNA and protein expressions are mapped from immunoblotting and RNA-seq data. Left half: before treatment; right half: after NADC treatment. During the pathogenesis and progression of IC, inflammatory and anti-inflammatory cytokines across these interconnected signaling pathways are varied to different extents, synergistically fostering the development of bladder inflammation. Precisely homing to inflamed sites and suppressing pain through NGF targeting, intravesical NADC effectively attenuates the activated inflammation-associated pathways and modulates cytokines, thereby relieving inflammation symptoms.